High-resolution investigations of Transverse Aeolian Ridges on Mars

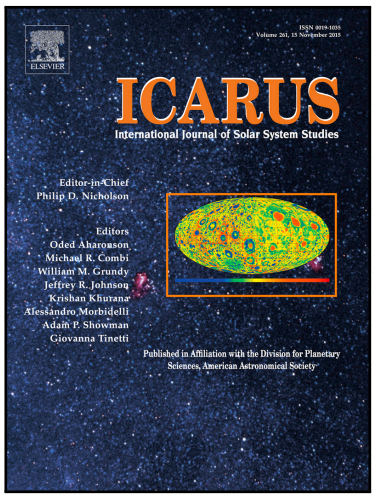

High-resolution Investigations of Transverse Aeolian Ridges on Mars

Daniel C. Berman , Matthew R. Balme , Joseph R. Michalski , Stacey C. Clark , Emily C.S. Joseph

PII: S0019-1035(17)30585-7
DOI: 10.1016/j.icarus.2018.05.003
Reference: YICAR 12891

To appear in: *Icarus*

Received date: 10 August 2017
Revised date: 19 December 2017
Accepted date: 4 May 2018

Please cite this article as: Daniel C. Berman , Matthew R. Balme , Joseph R. Michalski , Stacey C. Clark , Emily C.S. Joseph , High-resolution Investigations of Transverse Aeolian Ridges on Mars, *Icarus* (2018), doi: 10.1016/j.icarus.2018.05.003

Highlights

- Transverse Aeolian Ridges (TARs) on Mars are sourced from local deposits
- TARs are currently inactive and ancient
- TAR morphometries are consistent with terrestrial megaripples

High-resolution Investigations of Transverse Aeolian Ridges on Mars

Daniel C. Berman[1,*], Matthew R. Balme[2], Joseph R. Michalski[3], Stacey C. Clark[4], and Emily C.S. Joseph[1]

[1]Planetary Science Institute, 1700 E. Ft. Lowell Rd., Suite 106, Tucson, AZ 85719

[2]School of Physical Sciences, Open University, Milton Keynes, England, United Kingdom

[3]Department of Earth Sciences & Laboratory for Space Research, University of Hong Kong, Pokfulam, Hong Kong

[4]Department of Earth Sciences, Tennessee Technological University, Cookeville, TN 38505

*Corresponding author, bermandc@psi.edu, 520-382-0599

Keywords: Mars; Mars, surface; Aeolian processes

Abstract

Transverse Aeolian Ridges (TARs) are the most pervasive aeolian feature on Mars. Their small size requires high-resolution data for thorough analyses. We have utilized Mars Reconnaissance Orbiter (MRO) Context Camera (CTX) and High Resolution Image Stereo Experiment (HiRISE) images, along with MRO Compact Reconnaissance Imaging Spectrometer for Mars (CRISM) spectroscopic data to study TARs in detail. TAR deposits, along with related dark dune material and layered terrains, have been mapped in six study areas in order to identify sediment pathways and determine whether TARs are sourced locally or from global wind-born materials. TAR morphology and orientation were mapped in grids within each study area; the results show that TARs are probably locally sourced. We constructed four HiRISE Digital Terrain Models (DTMs) to measure TAR heights, widths, spacing, areas, symmetry, and to calculate sediment volumes. Results show that TARs have average heights of ~1.5 m, are very symmetrical, and are similar in form to terrestrial megaripples. Orthorectified HiRISE images taken 3 years apart were analyzed for TAR movement and none was found. Superposed craters on equatorial TARs give ages of ~2 Ma, suggesting that these are relatively ancient and generally inactive aeolian deposits. CRISM data were analyzed over TAR deposits, dark dune material, and light-toned terrains. Although the surfaces were somewhat obscured by dust cover, the results did not show any remarkable difference between TARs and other deposits. We conclude that TARs may be sourced from local materials and form in a similar way to terrestrial megaripples.

1. Introduction

Transverse Aeolian Ridges (TARs; Fig. 1a) –decameter-scale "ripple-like" aeolian bedforms – are one of the most common landforms on Mars (Zimbelman, 1987, 2008, 2010; Thomas et al., 1999; Bourke et al., 2003; Wilson and Zimbelman, 2004; Balme et al., 2005, 2006, 2008; Salvatore, 2008; Berman et al., 2011, 2012a, b, 2013, 2014, 2015; Kerber and Head, 2012; Zimbelman et al., 2013; Geissler, 2014; Sullivan et al., 2014; Zimbelman and Scheidt, 2014; Bridges et al., 2015; Foroutan and Zimbelman, 2016, 2017; Geissler and Wilgus, 2017; Hugenholtz et al., 2017). These features seem to represent a class of aeolian bedforms that is distinct from typical dune or ripple forms found on Earth. As the most widespread aeolian landform observable from orbit, TARs are clearly important for understanding meso- and small-scale interactions between the surface and atmosphere. TARs are also indicative of the weathering and sediment transport regime on Mars and an understanding of their morphologies, morphometries, and composition can provide information on the composition, mobility, and availability of aeolian sediments on Mars. Moreover, the spatial distribution of TARs provides information about where on Mars aeolian sediments are concentrated. If we can determine when TARs were active, and whether TARs are mobile under today's wind conditions, then we can begin to assess when and where TARs are/were active over Mars' recent geological history.

Thus TARs have the potential for being indicators of climate change on Mars. Aeolian processes are likely the dominant ongoing modification process of the Martian surface (e.g., Greeley et al., 1992; Wells and Zimbelman, 1997). The presence of aeolian bedforms indicates active coupling of the atmosphere with surface material and highlights regions that have experienced net deposition of sediment, or ongoing transport of sediment. Understanding aeolian transport on Mars is vital as there are currently few competing contemporary mechanisms for

transporting sedimentary material large distances. However, except for a few cases, we have little detailed knowledge of where sediment has accumulated, where it came from, what it is composed of, and how far it traveled before it got there.

Here we seek to further our understanding of aeolian processes and aeolian landforms on Mars. We concentrate on TARs and other similar-scale bedforms that have only been widely recognized in the high-resolution image data returned over the last decade or so. Many important questions regarding their emplacement mechanisms, age, sediment source, and mobility have arisen that demand further exploration. These questions have significance in terms of understanding the recent climate, understanding global sediment transport, and in possible future exploration of the planet, given that small dune-forms can be a hazard to rovers (as evidenced by the Opportunity Mars Exploration Rover becoming stuck for several weeks in large, coarse-grained ripples that morphologically resemble small TARs (e.g., Arvidson et al., 2011). TARs represent a fundamental piece of the global sediment budget/cycle and are therefore important to the sediment transport/storage story, and also may represent the best possibility to image evidence for mobility/active dune activity on Mars.

2. Science objectives

In this work we focus on the local/regional scale and thus have concentrated our study on several well-defined regional study areas to investigate the behavior of TARs in detail (Fig. 2). We seek to determine what factors control the morphology and morphometry of TARs by exploring sediment sources, climate, and local topography/geology as potential factors. In contrast to our previous studies (Balme et al., 2008; Berman et al., 2011) we are looking for local factors, as opposed to exploring global-scale datasets, to help constrain potential formation

mechanisms. We use infrared spectroscopy to determine the composition of TARs and test the hypothesis that TARs are derived from local sources by comparing the composition of the bedforms to that of the nearby bedrock. We search for evidence of compositional uniqueness within the TARs that could potentially contradict this hypothesis, and possibly be linked to a distal source region. By investigating stabilization ages of TARs and TAR fields (see Balme et al., 2008 for nomenclature), and how they move and evolve over time, we determine whether TARs are forming under current climate conditions, or are indicators of past climates. Finally, we explore the links between TARs and Large Dark Dunes (LDDs; Fig. 1b), comparing the compositions and morphologies of TARs that are both proximal to and distal to LDDs. We investigate how the presence of LDDs affects the formation of TARs – is one a source for the other? We also compare the infrared spectroscopy data of TARs and LDDs to investigate whether they are composed of the same materials.

3. Background and previous work

3.1. Dunes and ripples on Mars

Dunes were first identified on Mars from Mariner 9 images (McCauley et al., 1972; Cutts and Smith, 1973). Later, Mariner and Viking Orbiter images revealed a series of extensive ergs around the north polar ice cap (Cutts et al., 1976; Tsoar et al., 1979) and large dune fields in craters in the southern hemisphere (Cutts and Smith, 1973; Thomas, 1981; Lancaster and Greeley, 1987). Both the northern and southern dune fields are characterized by low albedo and large duneforms. Where dunes are coalesced, crest-to-crest wavelengths are typically hundreds to a few thousands of meters (Greeley et al., 1992). Bourke et al. (2008), Bridges et al. (2012),

and Chojnacki et al. (2015) have shown that martian dunes can be active under present day conditions and can move up to a few meters per year.

Ripples on the backs of martian dunes have typical wavelengths of ~3-6 m (Bridges et al., 2007) and are composed of sand size materials (Edgett and Christensen, 1991). Ewing et al. (2010) analyzed the spatial patterns of martian ripples and compared them to those of underlying dunes to compare resulting wind regimes, showing a highly complex relationship. These ripples have been shown to be currently active (e.g., Silvestro et al., 2010).

Sullivan et al. (2005, 2008) conducted in situ observations of ripples at the Mars Exploration Rover (MER) landing sites; Meridiani Planum ripples were composed of basaltic grains 50-125 μm in size and large, TAR-like coarse-grained megaripples were found in Gusev crater (see below). Lapotre et al. (2016) analyzed data from the Mars Science Laboratory (MSL) Curiosity rover of a type of ripple not seen on Earth; meter-scale wavelength asymmetric bedforms that resemble fluid-drag ripples.

3.2. TARs

As TARs are an order of magnitude smaller than LDDs, they can only be resolved in high-resolution orbital images (Zimbelman, 1987; Thomas et al., 1999). Balme et al. (2008) and Berman et al. (2011) focused on determining the large-scale distribution and concentration of TARs by analyzing all Mars Orbiter Camera (MOC) images (~10,000) within a pole-to-pole swath 45-degrees wide in longitude (from 0° - 45° E). For each image surveyed, the percent areal coverage of TARs was recorded and TARs in each image were categorized by morphology and topographic control. Relationships between TARs and other features such as LDDs were

recorded. Orientations of topographically independent TARs were measured and compared to General Circulation Model (GCM) data.

Building upon the preliminary classifications of TARs by Bourke et al. (2003) and Wilson and Zimbelman (2004), a new classification scheme was developed, as described in Balme et al. (2008). The scheme is based on: 1) The ridge-crest plan-view morphology, 2) the degree of topographic control of the TAR deposit, and 3) the size of the TAR deposit (e.g., sea, field, or patch). The aim of the classification scheme is to assist geographic analysis of TAR distribution and evolution. Using the three-part scheme, we can identify spatial variations in types of TARs, find areas where regional, rather than local, wind regimes shape TARs, and identify those areas with the largest TAR deposits.

3.3. TAR formation theories

In situ observations of gravel- or granule-mantled megaripples at the Spirit and Opportunity landing sites in Gusev crater and Meridiani Planum that resemble larger nearby TARs have led some to suggest that the TARs may also be granule-mantled megaripples (e.g., Sullivan et al., 2005, 2008, 2014; Balme et al., 2008). These megaripples are composed of a poorly sorted mix of sand and dust particles with some clasts and are indurated by a coating of larger granule-sized sediments. Laboratory experiments showed that granule ripples can form by larger particles sorting out and migrating through impact creep to coat the ripples (Bridges et al., 2015). De Silva et al. (2013) and Bridges et al. (2015) also describe megaripples in the Argentinian Puna as having similar morphometric and morphologic characteristics to martian TARs.

Zimbelman et al. (2012) and Zimberlman and Scheidt (2014) compared cross-sectional profiles of various terrestrial aeolian bedforms and found that reversing dunes most closely

resembled TARs in morphometry, given limited numbers of TAR statistics. Reversing dunes form under a bidirectional wind regime, where the two dominant wind directions are opposite in direction. Foroutan and Zimbelman (2016) and Hugenholtz and Barchyn (2017). analyzed orbital images of TAR-like bedforms in the Lut desert in Iran and found them to closely resemble TARs morphologically and morphometrically. Hugenholts and Barchyn (2017) further concluded that they are mega-ripples based on morphology, dynamics, and sedimentology.

An alternative hypothesis suggests that at least some TARs may be indurated dust deposits and that there is an evolution from dust drifts to various morphologies of TARs (e.g., Geissler, 2014). This hypothesis can explain certain characteristics of TARs, such as the brightness of TARs in relation to LDDs, and their low thermal inertia. A final point to note is that some TAR-like morphologies may be erosional forms eroded from bedrock ("Periodic Bedrock Ridges"; Montgomery et al., 2012), but these are thought to be different landforms than TARs.

Spatial associations between TARs, LDDs, layered and light-toned terrains have been previously noted (e.g., Balme at el., 2008). Kerber and Head (2012) described the presence of TARs in relation to the Medusa Fossae Formation – a very large, heavily eroded deposit of friable material that straddles the martian equatorial region (Bradley et al., 2002). Balme et al. (2008) and Berman et al. (2011) suggested that TARs are sourced from local LDDs and/or layered terrains. Although LDDs are much less pervasive on Mars than TARs (Hayward et al., 2007, 2014), eroding layered terrains are widespread (Malin and Edgett, 2000; Hynek and Phillips, 2008).

It is worth noting that there may be some overlap between small active dune ripples, large ripples such as those investigated by the Opportunity and Spirit rovers that are mostly inactive, and TARs, which are completely inactive. Meridiani plains ripples, like those at El Dorado in

Gusev (Sullivan et al., 2008), have been shown to be coarse-grained large ripples (~2-4 m wavelengths, ~30 cm tall) and are likely inactive, but within the same crest wavelength range as dark ripples found on dunes which are active almost planet wide and were characterized to be small TARs (Balme et al., 2017). The detection of annually migrating large ripples (~8-12 m wavelengths, ~1-2 m tall) in polar regions (Chojnacki et al., 2017) complicates this even further.

4. Methods

In this work we focus on the local/regional scale and thus have identified six regional study areas, each 5° by 5°, to investigate the characteristics and behavior of TARs in detail: two in the southern hemisphere (Study Areas 1 and 2), three near the equator (Study Areas 3-5), and one in the northern hemisphere (Study Area 6). These study areas were chosen on the basis of high TAR content and good image coverage, based on results from our previous study (Balme et al., 2008; Berman et al., 2011). All HiRISE and CTX (Malin et al., 2007) images for each study area were downloaded from the PDS Atlas, processed in ISIS3 software in the case of CTX, and ingested into an ArcGIS database.

4.1. Mapping of surficial deposits

Surficial sediment deposit maps of each study area have been produced using GIS software to investigate whether LDDs and TARs share sediment sources and pathways. For each of the study areas we have mapped the surficial deposits in terms of morphology, with a focus on sediment pathways (e.g., Ramsey et al., 1999; Bourke et al., 2004), sediment sources, and interactions/associations between TARs and LDDs. We have mapped the locations of: 1) TAR seas and fields, including orientations and whether they are saturated (i.e., no exposed bedrock

between bedforms), or "patchy" (i.e., bedrock is exposed between bedforms),) as well as morphological characteristics as described by Balme et al. (2008). 2) LDDs (Fig. 1b) and dark aeolian deposits that haven't accreted into discrete dune forms and have no slip faces, but do tend to have rippled surfaces (Fig. 1c), and 3) possible sediment sources (e.g., light-toned, layered terrains, Fig. 1d). By exploring sediment sources and local topography/geology as potential factors, we can constrain whether TAR-forming sediment is derived from nearby sources or globally, given the pervasiveness of TARs across the planet.

Study areas were subdivided into 15x15 km grids for classification according to morphology and orientation. TARs were assigned a morphological designation based on their plan-view crest structure according to first-order classifications developed by Balme et al. (2008): *simple, sinuous, forked, networked*, or *barchan-like*. Multiple TAR morphologies can exist within a single deposit and TARs within the same grid commonly display differing morphologies—for classification purposes, in these cases the dominant morphological form was catalogued with supplemental notes regarding any secondary morphologies present.

TAR orientation was analyzed grid by grid within each study area based on the azimuthal position of TAR ridge-crest bedform width (here ignoring grids dominated by networked TARs and those oriented radial to crater rims). Though more than one TAR orientation was often present within a given deposit, grid designations reflect the dominant plan-view TAR direction within the sampled area (N-S, NE-SW, NW-SE, or E-W).

4.2. Morphometric analyses

In order to determine what factors control the morphology and morphometry of TARs, we have produced four Digital Terrain Models (DTMs) from HiRISE stereo pairs in three of the

study areas for analysis that contain large numbers of saturated TARs. We have taken morphometric measurements for ~500 TAR bedforms within each DTM to compare them with terrestrial analog features and to assist in calculating TAR volumes in order to estimate their sediment budget.

DTMs were constructed from HiRISE stereo pairs using BAE Systems' SOCET SET 5.5 software according to the methodology described by Kirk et al. (2008) within Study Areas 1, 2, and 4 (center coordinates for DTM 1: -47.7°N, 31.0°E; DTM 2: -3.3° N, 12.9° E; DTM 3: -2.3° N, 11.8° E; and DTM 4: -46.9° N, 18.8° E) and used to analyze cross-sectional TAR elevation profiles. From these DTMs, profile graphs drawn perpendicular to TAR crests over the middle of each TAR enabled analysis of TAR morphometry (Fig. 3). DTMs have a horizontal resolution of 1 m/pixel and a vertical precision of ~0.1 m.

Elevation data from each measured profile were exported to MATLAB where the following measurements were extracted: height, profile width, area, wavelength, ripple index (height/wavelength), height/profile width, average slope, symmetry distance (i.e., the horizontal distance from the center point to the peak), bedform width, and symmetry index (symmetry distance/profile width). Note that the profile width (or bedform length) is perpendicular to the cross-wind bedform width as described by Balme et al. (2006). In order to calculate these values, first the point of the profile with maximum height (i.e., the TAR crest) was identified as $a_{max}(x,y)$. The outer margins of the TAR were defined as the lowest points of the profile on either side of this maximum, identified as $a_{min1}(x,y)$ and $a_{min2}(x,y)$. The profile width, w, was calculated as the difference in the x-values of these two points (Fig. 3a).

For the height and area calculations we wish to take into account the basal slope. A line that connected the two minima, y_{base}, was defined in order to represent this baseline surface using the

point-slope formula. The height, *h*, of the TAR was then found by subtracting the value of y_{base} at the point of the profile maximum from $a_{max}(y)$.

Similarly, the cross-sectional area *A* of the TAR was calculated by subtracting the area under the curve of y_{base} (A_2) from the total area under the profile (A_1). These two areas were calculated by trapezoidal numerical integration using MATLAB's *trapz* function.

Wavelengths were measured in ArcGIS as the distance from the crest of the TAR being measured to the crest of the nearest TAR. Ripple index is calculated as wavelength divided by height. To estimate TAR volumes, we used the bedform width of each measured TAR (parallel to the ridge crest), and multiplied that value by the cross-sectional area as calculated by the MATLAB script.

Symmetry distance was calculated by finding the distance between $a_{max}(y)$ and the midpoint of y_{base} (Fig. 3b). The symmetry ratio is the symmetry distance normalized to the profile width and is calculated by dividing the symmetry distance by the profile width. Average slopes were calculated following the method of Shockey and Zimbelman (2013) by taking the arc-tangent of twice the height divided by profile width.

4.3. Spectral data processing

Infrared observations from the Compact Reconnaissance Imagine Spectrometer for Mars (CRISM) were used to constrain the albedo and compositional properties of TARs, LDDs and local bedrock. In each of the study areas, targeted images were obtained; these include full resolution targeted images (FRT), which have 18 m/pix spatial resolution, half resolution long (HRL) images, which have 36 m/pixel spatial resolution, and half resolution short (HRS) images, which have 18 m/pixel spatial resolution, but smaller footprint than the FRT images. In all cases,

we focused on the L-channel data, which have a spectral range of 1.002 to 3.92 μm. Images were processed through a standard data pipeline using the CAT_ENVI toolkit provided by the CRISM team in order to correct for instrument effects, atmospheric effects, and calibrate to "I/F," which is comparable to surface reflectance. Note however that the atmospheric correction employed is a generalized approximation that does not take into account local viewing conditions at the time of data collection. As such, residual atmospheric effects remain; these features are not problematic in most cases.

Average spectra of areas of interest (e.g. LDDs) were ratioed against spectrally unremarkable terrains in the same image to produce ratio spectrum per typical CRISM data processing methods."These average spectra were compared to the spectra features of individual pixels over specific features (individual large dunes, for example) to be sure that the averaged spectra of regions of interest are representative of the actual surface materials.

Within the spectral range of the L-channel, we focused primarily on the 1-2.5 μm range because this range is more spectrally stable for CRISM and because these wavelengths contain more compositional information. The most useful electronic and vibrational absorptions in this range correspond to Fe^{2+} absorptions in pyroxenes and olivine, Fe^{3+} in oxides and hydroxides, and H_2O and OH vibrations in hydrated minerals. Some spectral summary products (mineral detection maps produced by the CRISM team) were used as a guide for some analyses, but all spectral analyses were based on observed, extracted surface spectra. Average albedo was calculated for using the 1.1 μm channel.

5. Results

5.1. Overall distribution of TARs, LDDS and possible source terrains

Our mapping (Figs. 4-9) shows that in the southern and northern mid-latitudes, TARs are mostly found near LDDs or dark aeolian deposits, and nearly all of the deposits are found in local topographic lows, or sediment traps. The equatorial study areas (3-5) are heavily blanketed with TARs and show strong association with layered terrains. Transport pathways appear to be primarily constrained by local topography. Across the six study areas, saturated seas, fields, and patches of TARs cover an area of 99,000 square kilometers (or ~22% of the entire area); patchy fields of TARs, defined as regions that have distinct clusters of TARs interspersed in areas without TARs, cover an area of 65,000 square kilometers (~14%).

LDDs and dark aeolian deposits tend to lie directly on top of TAR deposits on crater floors. In the equatorial regions, dark aeolian deposits are also found on flat areas adjacent to layered terrains. LDDs in all six study areas cover an area of ~12,000 km^2 (~3%), while dark aeolian deposits cover an area of ~39,000 km^2 (~9%).

Light-toned terrains exhibit diversity throughout the various study regions, but are generally equally bright or brighter than nearby TARs. These terrains often exhibit layered outcrops with alternating dark layers. ~42,000 km^2 of light-toned terrains were mapped throughout the six study areas.

The type noted as "simple" accounts for the overwhelming majority of TAR morphology, comprising 817 of the 1194 grids analyzed, or ~68% of the mapped TARs. Only in Study Area 3 are simple TARs outnumbered by those with barchan-like morphologies.

Analysis of TAR orientations shows a predominantly N-S orientation in four of the six study areas—Study areas 1 and 2 in the mid-southern and Study areas 3 and 4 in the equatorial latitudes—while TARs within the Study area 5 in the equatorial latitude and Study area 5 in the mid-northern latitudes adopt predominantly W-E and NW-SE orientations, respectively. The

consistency of similar TAR orientations across large areas suggests that TAR formation is driven primarily by large-scale wind patterns. These results are consistent with those from General Circulation Models for present Martian obliquities (e.g., Berman et al., 2011).

5.2. Analysis of individual study areas

Study Area 1 (-50 – -45°N; 27 – 32°E; Fig. 4) is centered around Proctor crater, a 160 km diameter impact basin with a prominent field of LDDs, one of the largest on Mars (~2800 km^2 in area), on its eastern floor (Fenton et al., 2003, 2005). Around this field is a large sea of TARs, ~7700 km^2 in area. TARs in this sea are closely spaced, have simple to sinuous/forked planform morphologies (Figs. 1a, 4b) and are interspersed with ~1-10 m scale boulders (cf., Fig. 1a). TAR orientations in this region trend primarily north-south or northwest-southeast (Fig. 4c).

The western side of the crater floor is marked by a complex of large pits (Fig. 4a,d) that exhibit distinct layers at their margins. Many of these layers are composed of polygonally-fractured bright outcrops with polygonal fractures ~5-10 m in diameter that can be discerned in HiRISE images (Fig. 4e,f). The bedrock zones outlined by these fractures can be seen detaching from the margins to form discrete boulders (Fig. 4f). Dark aeolian material can also be seen emanating from these layers; at HiRISE scale, the surface of this material contains meter-scale ripples. The floors of the pits are also blanketed with topographically controlled TARs. Additionally, there are several smaller craters surrounding Proctor, including Rabe crater that contain their own LDD and TAR fields as well as layered pits.

Study Area 2 (-49 – -44°N; 16 – 21°E; Fig. 5) is centered around Kaiser crater, a 190 km diameter impact basin. Small patches of TARs are observed in local lows throughout the study area. Morphologically, TARs in this study area are predominantly simple, with a small number

being sinuous (Fig. 5b). The 100 km-diameter crater just to the north of Kaiser (outside of the study area) also has an LDD field, a large pit with layered outcrops, and TARs. TAR orientations in this region trend primarily north-south (Fig. 5c).

On the southern floor of Kaiser, a large LDD field (Fig. 5a) surrounds a ~500 m thick mound of eroding light-toned material (Fig. 5d-f); this deposit appears to extend beneath the LDD field and to the northeast.. A patchy field of TARs surrounds the LDD field. HiRISE scale images also reveal that, superposing the light-toned material, are TARs with large wavelengths and which are themselves surrounded by bright, unconsolidated, potentially TAR-forming sediment (Fig. 5e). Several of the TARs in this image have wind shadows behind them, where the bright material has not been deposited. In an adjacent image (Fig. 5f), trails of potential TAR-forming sediment can be seen leading from bright outcrops to TAR deposits, which tend to form in front of topographic obstacles where the sediment has built up.

Study Area 3 (-1 – 4°N, -3 – 2°E; Fig. 6) in Meridiani Planum is topographically very flat and contains vast seas of TARs (Fig. 6a). There are a few LDD fields within some of the larger craters in this study area as well as extensive fields of dark aeolian deposits. As noted by Balme et al. (2008), there is a strong association in this region between TARs and light-toned outcrops (Fig. 6d), which cover vast areas in this study area (~35,000 km^2).

76% of the grids with TARs in this area are primarily composed of barchan-like TARs, with the rest generally being of simple morphology (Fig. 6b,d). TAR orientations in this region trend primarily north-south or northeast-southwest (Fig. 6c). In some areas, simple TARs and barchan-like TARs are intermixed (Fig. 6c); Figure 6d shows barchan-like TARs on top of the lower strata of light-toned material, with simple TARs on upper strata., Fig. 6e shows a phenomenon unique to this region where chains of barchan-like TARs that, at lower resolution, could be

mistaken for a single simple TAR with perpendicular orientation (Fig. 6c,e). A similar phenomenon was also observed in the Lut desert on Earth (Hugenholtz and Barchyn, 2017). Figure 6f shows a crater impacted into light-toned layered deposits; dark aeolian material can be observed eroding from the layers on the crater walls and flowing to the floor, which is covered by networked TARs.

Study Area 4 (-5 – 0°N, 10 – 15°E; Fig. 7) encompasses the western edge of Schiaparelli crater (450 km) and surrounding terrains and contains large seas of TARs (Fig. 7a). The TARs in this region tend to be very small, sometimes only discernible in HiRISE images. Morphologically, they are a mix of barchan-like (primarily outside of Schiaparelli crater) and simple TARs (Fig. 7b). TAR orientations in this region vary between north-south, northwest-southeast, and northeast-southwest (Fig. 7c).This region has smaller deposits of LDDs and dark aeolian material. Light-toned eroded units are scattered throughout the study area, mainly on crater floors (Fig. 7d,f). Some simple TARs in this region exhibit secondary ridges (i.e., "feathered" morphology, cf. Bourke et. al, 2003), and even tertiary ridges (Fig. 7d).

Study Area 5 (-11 – -6°N, 34 – 39°E; Fig. 8) includes most of Dawes crater (180 km) and terrain to the west. Unlike the other equatorial study areas, this study area has no obvious eroding layered or light-toned terrains, yet does have widespread, if patchy, TAR deposits (Fig. 8a). An LDD field lines the southern wall of the crater and dark aeolian deposits are found throughout the study area. TARs are primarily simple, with some barchan-like examples on the floor of Dawes crater (Fig. 8b). TAR orientations in this region trend primarily west-east or northeast-southwest (Fig. 8c). Some have a "feathered" appearance with deflated primary ridges and prominent secondary ridges (Fig. 8d).

Study Area 6 in the northern mid-latitudes (39 – 44°N, 42 – 47°E; Fig. 9) is centered around the 130 km-diameter Moreux crater. LDDs and dark deposits surround the crater's central peak, with adjacent patchy TAR fields extending across the northern floor and around the peak (Fig. 9a). Small TAR patches are also observed on channel floors west of the crater. TARs in this region are primarily simple in morphology, with a small number of barchan-shaped bedforms (Fig. 9b). TAR orientations in this region trend primarily west-east or northwest-southeast (Fig. 9c).TAR deposits are fairly patchy and underlie the LDDs (Fig. 9d).

5.3. Morphometric results

Our results show TARs to be small, with average median heights of 1.3 m, profile widths of 22.8 m, and wavelengths of 35.6 m. These values are generally consistent with previous population studies (Bourke et al., 2006; Zimbelman, 2010; Shockey and Zimbelman, 2013; Foroutan and Zimbelman, 20017; Geissler and Wilgus, 2017; Hugenholtz et al., 2017). Our analysis found TAR cross-sectional profiles to be extremely symmetric, with median symmetry ratios of 0.05, 0.05, 0.10, 0.06 for DTMs 1, 2, 3, and 4 respectively. TAR flank slopes range from ~3-10°. Ripple indexes for all four sites are generally high (median of ~28) as compared to terrestrial granule ripples; Sharp (1963) gives a mean ripple index of 15 for granule ripples in Kelso Dunes. Sharp (1963) found that generally grain size decreased as ripple index increased. Full results are shown in Table 1.

When TAR heights are scaled by profile width to give an aspect ratio, the TARs in DTMs 1, 2, and 4 have aspect ratios within the values measured for terrestrial megaripples and transverse dunes (but not reversing dunes), while profile widths are intermediate between the two types (Zimbelman et al., 2012; Shockey and Zimbleman, 2013); aspect ratios for DTM 3 (barchan-like

TARs) show a much wider range, but median values are consistent with the other regions (Fig. 10a). When TAR heights and profile widths are both scaled by profile width (Fig. 10b), average values for the median scaled heights for all four DTMs are ~0.05, consistent with transverse dunes or megaripples, but not with reversing dunes, which have scaled heights closer to 0.14 (Zimbelman et al., 2012).

Elevation profiles and wavelengths have been measured for 550 TAR bedforms in DTM A (Fig.11), on the floor of Proctor crater in Study Area 1. TAR heights range from 0.1 m to 3.7 m. The median TAR height is 1.9 m (25^{th} percentile 1.6 m/75^{th} percentile 2.2 m); the median profile width (parallel to inferred transport direction) is 30.2 m (26.6/35.2); median wavelength is 51.5 m (40.1/63.1); median ripple index is 27.2 (22.4/33.8); and the median height/profile width ratio is 0.06 (0.05/0.07). TAR bedform widths (parallel to the ridge crest) and areas were used to estimate sediment volume within the DTM, and then extrapolated to the entire Proctor crater TAR field to give a total volume of TARs in this study area of ~1.7×10^6 m^3.

DTM B (Fig. 12) is in Study Area 4 along the rim of Schiaparelli crater. TARs in this DTM are simple in morphology, but appear highly degraded and indurated and could be mistaken for periodic bedrock ridges (e.g., Montgomery et al., 2012). Inter-bed regions appear devoid of aeolian materials. 507 elevation profiles were measured on this DTM. TAR heights range from 0.1 to 3.5 m and the median height is 1.6 m (1.3/2.0). Median profile width is 25.2 m (20.9/29.8), median wavelength is 42.6 m (35.8/50.2), median ripple index is 25.5 (20.7/33.4), and median height/profile width is 0.06 (0.06/0.07).

The TARs in DTM C (Fig. 13) in Study Area 4 are primarily barchan-like in morphology and generally have small heights, profile widths, bedform widths, and wavelengths. 500 individual TARs were measured in this DTM. The median height for these TARs is 0.3 m (0.2/0.5), with a

range of 0.1 m to 3.3 m. Median profile width is 9.5 m (8.3/11.3). TARs here are closely spaced and have median wavelengths of 9.7 m (7.8/12.2). Median ripple index is 30.6 (20.6/44.2) and median height/profile width is 0.03 (0.02/0.05).

Five hundred three measurement profiles were made of TAR bedforms in DTM D (Fig. 14) in Kaiser crater in Study Area 2. The TARs in this DTM have simple morphologies, but have a large diversity of sizes and wavelengths due to topographic variations (e.g., the presence of a crater) compared to the Proctor DTM, which covers a topographically flat and low relief area. TARs confined to the floor of the 7 km diameter crater Moni, where more aeolian material can be trapped, tend to be much larger in this study area than TARs at the margins of the crater. Thus, topographic control influences TAR size. Heights in the DTM range from 0.1 m to 10.0 m. The median height is 1.5 m (0.9/2.1); the median profile width is 26.4 m (20.5/34.8); median wavelength is 38.7 m (27.8/62.2); median ripple index is 28.1 (19.3/41.0); and the median height/profile width ratio is 0.05 (0.04/0.07).

5.4. Crater counting and changes in high-resolution images

Aeolian bedforms such as dunes and ripples have been shown to be moving across the surface globally at rates of 0.4 to 9 m per year by analyzing time-series high-resolution images (Chojnacki et al., 2011, 2015; Bridges et al., 2012). TARs, however have not been observed to have any motion during observable timescales of 6-9 Earth years (e.g., Bridges et al., 2012; Chojnacki et al., 2014, 2015, 2017). We analyzed two separate overlapping orthorectified HiRISE images (ESP_014100_1600 and ESP_028526_1600) taken 3 Earth years apart but, like previous studies, found no evidence of movement. The images were orthorectified at 25 cm/pixel to a corresponding DTM, and no changes were observed at more than ~4 pixels. In the areas we

studied, at least, TARs represent a stable bedform that is clearly less mobile than other aeolian deposits.

We have searched for superposed craters over all of the mapped contiguous TAR fields throughout the study areas in HiRISE and CTX images in order to estimate stabilization ages (e.g., Reiss et al., 2004). TARs in the equatorial study areas do contain superposed craters, and crater counts on several different regions in Study Areas 3 and 4 were possible. Following the methodology of Hartmann (2005, 2007a,b), impact craters were identified and the diameters of craters superposed on TAR bedforms were measured, within the resolution limits (down to ~5 m). In order to access a wider diameter range (e.g., Hartmann, 2005, 2007a,b), counts were conducted within large regions in both study areas on CTX images (e.g., Figure 15a) as well as subsets on higher-resolution HiRISE images (e.g., Figure 15b) Crater size-frequency distributions (SFD) were then plotted on the isochron system of Hartmann (2005).

The potential for "contamination" by secondary craters and thus erroneous age estimates from small crater sizes (i.e., ≤ ~300 m in diameter) is widely recognized (e.g., Hartmann, 2005, 2007a,b; McEwen and Bierhaus, 2006). Distributed "background" secondaries (i.e., those not included in rays, chains, or clusters) are not excluded from our counts as the production function used to determine the isochrons includes both primaries and these background secondaries [Hartmann, 2005]. If the number of background secondaries included in the counts exceeded those of the production function, one would expect that below a certain diameter, the SFD slope would exceed the isochron (production function) slopes. As shown in Fig. 15c, this only happens in the counts of HiRISE image PSP_009555_1815 at diameters below ~30 m. Results between CTX and HiRISE resolutions are consistent with each other over a diameter range of ~30 m to

~200 meters, and both regions show approximately the same model crater retention ages of ~2 Ma.

Mid-latitude TAR deposits generally have no superposed craters. In order to estimate a maximum crater retention age for a large deposit with no craters, such as the TAR sea around the Proctor crater LDD field, we use a hypothetical situation: what if this area has only a single crater of a size large enough to be recognized in CTX? What would the 'single-crater' crater retention age be (see Balme et al., 2008; Berman et al., 2011)? In our data, the observations of zero such craters would mean that the true crater retention age could be no older than the age given from the single crater age. The resulting crater retention ages are ~100,000 – 500,000 years for this TAR sea, consistent with previous estimates for TARs (Berman et al., 2011) and Meridiani megaripples (Golombek et al., 2010.

5.5. Compositional analyses

Limited compositional studies have been carried out to attempt to: 1) characterize the basic spectral characteristics of TARs and LDDs, 2) constrain the composition of TAR materials themselves, and 3) compare the composition of TARs to the composition of local LDDs and to local layered terrains (or other terrain units).

CRISM analyses of saturated TAR fields and LDDs quantify the albedo and compositional characteristics of the deposits. TARs are distinctly brighter and are more variable in albedo than LDDs, with the brightest TARs having albedos of ~0.36 (Dawes crater, Study Area 5) and the darkest ~0.13 (Kaiser crater, Study Area 2, and Meridiani Planum, Study Area 3). The brightest LDDs are ~0.22 (Schiaparelli crater, Study Area 4) and the darkest are ~0.10 (Kaiser Crater).

Spectral analyses over saturated TARs, LDDs, and local bedrock in Study Area 3 (Meridiani Planum) are shown in Figure 16 and in Study Area 2 (Kaiser crater) in Figure 17. In general, CRISM results show that the TARs and LDDs in this region are both "spectrally unremarkable." In other words, these surfaces typically have no diagnostic spectral features. Such surface spectra are not uncommon for dark regions and while these data are not indicative of any particular mineralogy, they are consistent with the presence of a dust coating. Dune spectra in Kaiser crater contain a weak, broad Fe^{2+} absorption attributable to pyroxene (Fig. 17).

In Meridiani, spectroscopic data do not show any obvious characteristics of TARs or LDDs that might be associated with formation or preservation processes. There are no mineral indicators of cementing agents (e.g. enrichment in salts or ices). The local bedrock contains spectral absorptions related to clay minerals (Figure 16) or sulfates, which are not observed in the dunes. In the case of phyllosilicates, this is not surprising as clays might be swept away in suspension by the wind after being eroded from local bedrock. However, the TARs' composition is not distinguishable from that of the local bedrock. There is no evidence for olivine or other potential mineral tracers that might be segregated due to density.

TAR deposits in Study Area 2 (Fig. 17) exhibit strong spectral slopes, which might indicate the presence of grain coatings. Chlorides could be a candidate cementing agent and if they exist in 10% of perfect abundance, they should be detectable in CRISM data or thermal infrared data. It has been demonstrated that chlorides show a positive spectral slope CRISM data, but the spectra for TARs have a negative slope. In addition, chlorides only exhibit those features in other deposits (Jensen and Glotch, 2011) because they compose a large fraction of the deposit by volume and in the case of TARs or LDDs, they would only be present in small abundances. Lastly, Mars Odyssey Thermal Emission Imaging System (THEMIS) decorrelation stretch

images (e.g., Fergason et al., 2006) do not show obvious spectral differences among or between deposits at the 100 m/pixel scale, which potentially argues against the presence of chlorides and against fundamentally different mineralogy between TARs or LDDs and their surrounding terrains.

6. Discussion

So what are TARs? Morphometric analyses show that most TARs resemble terrestrial megaripples more than they do reversing dunes and, in general, this is a solid analog. It is possible that TARs in certain regions such as Syria Planum may be eroded, indurated dust deposits (Geissler, 2014), but in general, eroded dust deposits are not a strong analog for most TARs on Mars. Geissler (2014) suggests that a global source of dust can explain the widespread nature of TARs; however, we have shown that that there are abundant local sediment sources for the TARs we have studied.

Results from sediment mapping (Figs. 4-9) and demonstrate that there are potential localized sources for TAR-forming sediment in most of the study areas. For the TARs in and around Proctor crater (Study Area 1, Fig. 4), TARs may source from the LDDs and/or the eroding layered terrain on the western edge of the crater, or from eroding terrains in nearby craters. Given wind patterns from GCMs in this study area (Berman et al., 2011), a potential sediment pathway exists from the pits to the LDD and TAR fields on the east side of the crater floor, which sit at a low elevation point on the crater floor (see green arrows in Fig. 4a). TARs in Kaiser crater (Study Area 2, Fig. 5) surround a large LDD deposit and a large mound of light-toned material, and likely source from either or both; sediment can directly be observed trailing from the light toned material to TARs (Fig. 5e). In Meridiani Planum (Study Area 3, Fig. 6),

widespread eroding layered terrains provide a likely TAR sediment source. The Schiaparelli crater study area (Study Area 4, Fig. 7) has fewer LDDs but does have widespread dark aeolian deposits, as well as patches of layered terrains on the northern edge of the crater and on the floor of the smaller crater just west of Schiaparelli near the TAR desposits. TARs in the Dawes crater study area (Study Area 5, Fig. 8) may have sourced sediment from the LDDs and dark deposits on the southern crater floor as well as to the northwest of the crater. The TARs in Moreux crater may have sourced from the LDDs and dark deposits on the crater's floor, especially given that there are few, if any TARs outside of the crater. Most of the large TAR deposits in these study areas lie either on the floors of craters or on large flat plains, indicating that TAR deposits settle into local topographic lows. There is no evidence for the necessity of global scale transport that moves material across vast distances to form TARs.

Crater counts show that most TARs stabilized at least 100,000 years ago (2 million years ago for equatorial TARS) and may have formed much earlier. From this we can conclude that TARs may have formed under different climate conditions. This is important when considering formational/depositional mechanisms and when applying atmospheric modeling to TARs.

The differences in albedo and thermal inertia between TARs and LDDs are likely due to differences in grain size given the similarities in their spectral characteristics. Therefore they likely share a common source and their differences are due to sorting. Although LDDs are active and younger, they are not necessarily recent landforms and may be long-lived features that have taken thousands of years to evolve to their current state. LDD and TAR-forming sediment both may be derived from nearby eroding terrains. We suggest that TARs and LDDs form from the same source and grains of different sizes are sorted out and distributed between the two landforms. As the LDDs are likely composed of finer grains (e.g., Edgett and Christensen, 1991),

they remain active over long periods of time, while the larger particles potentially coating the TARs lead to induration and immobilization.

7. Conclusions

1) Sediment mapping indicates that sediment sources for TARs are local and often co-located with LDDs and eroding layered terrains, which are likely sediment sources.

2) TARs are compositionally similar to local bedrock, supporting the conclusion that they are locally sourced.

3) TARs appear to be currently inactive and are relatively ancient – several million years at least. Some very extensive TAR fields could have been active more recently, perhaps up to 100,000 years, yet are still younger than the LDDs.

4) Our DTM studies show that, in general, TARs have heights of ~0.5 to ~2.5 m, across-bedform widths of ~15 to ~35 m, flank slopes of ~3-10°, and ripples indices that are between 1 and 60.

5) The morphometry of TARs based on a large sample is more consistent with a megaripple origin than formation as reversing dunes.

Acknowledgements

This research was supported by a grant #NNX11AI82G from NASA's Mars Data Analysis Program. MRB was supported also by grants from UK Space Agency (ST/F012020/1) and the UK Leverhulme Trust (RPG-397). Thanks to Matt Chojnacki and Jim Zimbelman for the substantive and helpful reviews. Special thanks also to the late Nathan Bridges for very helpful discussions over the years. All CTX images credit: NASA/JPL/MSSS. All HiRISE images credit: NASA/JPL/UA. ALL CRISM images credit: NASA/JHU/APL.

Table 1. TAR morphometries

	DTM A (n=550)	**DTM B (n=507)**	**DTM C (n=500)**	**DTM D (n=503)**	
Study Area	1	4	4	2	
Height (m)					**Average 1-4**
Mean	1.9	1.6	0.5	1.8	**1.5**
Median	1.9	1.6	0.3	1.5	**1.3**
25th percentile	1.6	1.3	0.2	0.9	**1.0**
75th percentile	2.2	2.0	0.5	2.1	**1.7**
Min	0.1	0.1	0.1	0.1	**0.1**
Max	3.7	3.5	3.3	10.0	**5.1**
Profile Width (m)					
Mean	31.2	25.5	10.0	31.3	**24.5**
Median	30.2	25.2	9.5	26.4	**22.8**
25th percentile	26.6	20.9	8.3	20.5	**19.1**
75th percentile	35.2	29.8	11.3	34.8	**27.8**
Min	1.9	8.7	4.0	8.2	**5.7**
Max	56.0	43.6	26.9	142.9	**67.3**
Area (m^2)					
Mean	329.3	250.8	245.4	643.8	**367.3**
Median	325.8	247.4	250.2	667.9	**372.8**
25th percentile	184.4	140.1	122.9	351.3	**199.7**
75th percentile	471.4	350.1	359.9	924.2	**526.4**
Min	26.2	12.8	0.0	14.4	**13.3**
Max	624.1	619.0	553.7	1532.9	**832.4**

Bedform Width (m)					
Mean	105.1	199.8	30.1	103.7	**109.7**
Median	95.7	176.2	26.0	87.4	**96.3**
25th percentile	72.2	124.8	20.2	58.2	**68.9**
75th percentile	127.9	247.5	36.6	128.3	**135.1**
Min	17.9	44.6	6.4	18.9	**21.9**
Max	374.8	728.6	115.8	487.6	**426.7**
Volume (m^3)					
Mean	34647.4	49090.2	7281.6	70052.2	**40267.9**
Median	29218.1	39444.3	6062.8	48700.3	**30856.3**
25th percentile	16211.8	20724.5	3123.1	27395.4	**16863.7**
75th percentile	45820.6	63140.3	9759.2	84280.6	**50750.1**
Min	2476.7	1271.1	0.6	1147.9	**1224.1**
Max	174506.9	323359.0	29806.7	625372.6	**288261.3**
Wavelength (m)					
Mean	53.0	44.5	10.7	51.4	**39.9**
Median	51.5	42.6	9.7	38.7	**35.6**
25th percentile	40.1	35.8	7.8	27.8	**27.9**
75th percentile	63.1	50.2	12.2	62.2	**46.9**
Min	19.9	18.4	4.0	11.9	**13.5**
Max	125.2	105.8	34.0	248.6	**128.4**
Ripple Index (λ/h)					
Mean	29.8	30.3	34.1	42.1	**34.1**
Median	27.2	25.5	30.6	28.1	**27.9**

25th percentile	22.4	20.7	20.6	19.3	**20.8**
75th percentile	33.8	33.4	44.2	41.0	**38.1**
Min	11.1	10.4	2.8	6.8	**7.8**
Max	286.2	342.4	146.7	877.7	**413.3**
Height/Profile Width					
Mean	0.06	0.06	0.05	0.05	**0.06**
Median	0.06	0.06	0.03	0.05	**0.05**
25th percentile	0.05	0.06	0.02	0.04	**0.04**
75th percentile	0.07	0.07	0.05	0.07	**0.06**
Min	0.01	0.00	0.01	0.01	**0.01**
Max	1.01	0.12	0.45	0.18	**0.44**
Symmetry Distance (m)					
Mean	1.9	1.4	1.0	2.1	**1.6**
Median	1.5	1.0	1.0	1.5	**1.2**
25th percentile	0.5	0.5	0.5	1.0	**0.6**
75th percentile	2.9	2.0	1.4	2.9	**2.3**
Min	0.0	0.0	0.0	0.0	**0.0**
Max	9.9	6.6	3.5	13.0	**8.2**
Symmetry Ratio					
Mean	0.06	0.05	0.11	0.07	**0.07**
Median	0.05	0.05	0.10	0.06	**0.07**
25th percentile	0.02	0.02	0.06	0.03	**0.03**
75th percentile	0.09	0.08	0.17	0.10	**0.11**
Min	0.00	0.00	0.00	0.00	**0.00**
Max	0.24	0.23	0.30	0.34	**0.28**

Height/Wavelength					
Mean	0.04	0.04	0.05	0.04	**0.04**
Median	0.04	0.04	0.03	0.04	**0.04**
25th percentile	0.03	0.03	0.02	0.02	**0.03**
75th percentile	0.04	0.05	0.05	0.05	**0.05**
Min	0.00	0.00	0.01	0.00	**0.00**
Max	0.09	0.10	0.36	0.15	**0.17**
Slope					
Mean	7.0	7.4	5.4	6.2	**6.5**
Median	7.1	7.3	3.8	6.1	**6.1**
25th percentile	6.0	6.5	2.7	4.5	**4.9**
75th percentile	7.9	8.1	5.6	7.5	**7.3**
Min	0.6	0.5	0.9	0.8	**0.7**
Max	63.7	13.4	41.7	19.6	**34.6**

References

Arvidson, R.E., W. Ashley, J.F. Bell III, M. Chojnacki, J. Cohen, T.E. Economou, W.H. Farrand, R. Fergason, I. Fleischer, P. Geissler, R. Gellert, M.P. Golombek, J.P. Grotzinger, E.A. Guinness, R.M. Haberle, K.E. Herkenhoff, J.A. Herman, K.D. Iagnemma, B.L. Jolliff, J.R. Johnson, G. Klingelhöfer, A.H. Knoll, A.T. Knudson, R. Li, S.M. McLennan, D.W. Mittlefehldt, R.V. Morris, T.J. Parker, M.S. Rice, C. Schröder, L.A. Soderblom, S.W. Squyres, R.J. Sullivan, and M.J. Wolff, 2011. Opportunity Mars rover mission: Overview and selected results from Purgatory ripple to traverses to Endeavour crater. J. Geophys. Res. Planets, 116(R7), doi:10.1029/2010JE003746.

Balme, M.R. and M.C. Bourke, 2005. Preliminary results from a new study of Transverse Aeolian Ridges (TARs) on Mars, LPSC XXXVI [CDROM].

Balme, M.R., D.C. Berman, and M.A. Bourke, 2006. Transverse Aeolian Ridges on Mars, International conference on Aeolian Research, Guelph, Canada.

Balme, M.R., D.C. Berman, M.C. Bourke, and J.R. Zimbelman, 2008. Transverse Aeolian Ridges on Mars. Geomorphology 101, 703-720.

Balme, M., E. Robson, R. Barnes, F. Butcher, P. Fawdon, B. Huber, T. Ortner, G. Paar, C. Traxler, J. Bridges, S. Gupta, and J.L. Vago, 2017. Surface-based 3D measurements of small aeolian bedforms on Mars and implications for estimating ExoMars rover traversability hazards. Planet. Space Sci., https://doi.org/10.1016/j.pss.2017.12.008.

Berman, D.C., M.R. Balme, S. Rafkin, and J.R. Zimbelman, 2011. Transverse Aeolian Ridges (TARs) on Mars II: Distributions, orientations, and ages. Icarus 213, 116-130, doi:10.1016/j.icarus.2011.02.014.

Berman, D.C. and M.R. Balme, 2012a. Investigations of Transverse Aeolian Ridges on Mars, Lunar Planet. Sci. Conf. 43, abstract 1598, 2012.

Berman, D.C., M.R. Balme, and T.I. Michaels, 2012b. Investigations of Transverse Aeolian Ridges on Mars, Third International Planetary Dunes Workshop, LPI Contribution No. 1673, abstract 7025.

Berman, D.C., M.R. Balme, J.R. Michalski, and T.I. Michaels, 2013. Further investigations of Transverse Aeolian Ridges on Mars, Lunar Planet. Sci. Conf. 44, abstract 2359.

Berman, D.C. and M.R. Balme, 2014. Transverse Aeolian Ridges on Mars: Sediment sources, volumes and ages, AGU Fall Meeting, abstract P33A-4022.

Berman, D.C., J.R. Michalski, and M.R. Balme, 2015. Analyses of Transverse Aeolian Ridges on Mars, Lunar Planet. Sci. Conf. 46, abstract 2210.

Bourke, M.C., S.A. Wilson, and J.R. Zimbelman, 2003. The variability of TARs in troughs on Mars, LPSC XXXIV [CDROM].

Bourke, M.C., J.E. Bullard, and O.S. Barnouin-Jha, 2004. Aeolian sediment transport pathways and aerodynamics at troughs on Mars. J. Geophy. Res., 109(E07): doi:10.1029/2003JE002155.

Bourke, M.C., M. R. Balme, R. A. Beyer, K.K. Williams, and J. Zimbelman, 2006. A comparison of methods used to estimate the height of sand dunes on Mars. Geomorphology, 81(3-4): 440-452.

Bourke, M.C., K.S. Edgett, and B.A. Cantor, 2008. Recent aeolian dune change on Mars, Geomorphology 94, 247-255.

Bradley, B.A., S.E.H. Sakimoto, H. Frey, and J.R. Zimbelman, 2002. Medusae Fossae Formation: new perspectives from Mars Global Surveyor, J. Geophys. Res. 107(E8).

Bridges, N.T., P.E. Geissler, A.S. McEwen, B.J. Thomson, F.C. Chuang, K.E. Herkenhoff, L.P. Keszthelyi, and S. Martínez-Alonso, 2007. Windy Mars: A dynamic planet as seen by the HiRISE camera. Geophys. Res. Lett. 34. doi:10.1029/2007GL031445.

Bridges, N.T., M.C. Bourke, P.E. Geissler, M.E. Banks, C. Colon, S. Diniega, M.P. Golombek, C.J. Hansen, S. Mattson, A.S. McEwen, M.T. Mellon, N. Stantzos, and B.J. Thomson, 2012. Planet-wide sand motion on Mars, Geology 40(1), 31-34.

Bridges, N.T., M.G. Spagnuolo, S.L. de Silva, J.R. Zimbelman, and E.M. Neely, 2015. Formation of gravel-mantled megaripples on Earth and Mars: Insights from the Argentinean Puna and wind tunnel experiments, Aeolian Res. 17, 49-60.

Chojnacki, M. D.M. Burr, J.E. Moersch, and T.I. Michaels, 2011. Orbital observations of contemporary dune activity in Endeavor crater, Meridiani Planum Mars, J. Geophys. Res. 116(E7).

Chojnacki, M., D.M. Burr, and J.E. Moersch, 2014a. Valles Marineris dune fields as compared with other martian populations: Diversity of dune compositions, morphologies, and thermophysical properties. Third Planet. Dunes Syst. 230, 96–142. doi:10.1016/j.icarus.2013.08.018.

Chojnacki, M., D.M. Burr, J.E. Moersch, and J.J. Wray, 2014b. Valles Marineris dune sediment provenance and pathways. Icarus 232, 187–219. doi:10.1016/j.icarus.2014.01.011.

Chojnacki, M., J.R. Johnson, J.E. Moersch, L.K Fenton, T.I. Michaels, and J.F. Bell, 2015. Persistent aeolian activity at Endeavour crater, Meridiani Planum, Mars; new observations from orbit and the surface, Icarus 251, 275-290.

Chojnacki, M., M.E. Banks, and A. Urso, 2017. Global Extremes in Martian Bedform Migration and Sand Flux Rates, in: Fifth International Planetary Dunes Workshop. Lunar and Planetary Institute, Houston, p. Abstract #3033.

Cutts, J.A. and R.S.U Smith, 1973. Aeolian deposits and dunes on Mars. J. Geophy. Res., 78: 4139-4154.

Cutts, J.A. K.R. Blasius, G.A. Briggs, M.H. Carr, R. Greeley, and H. Masursky, 1976. North polar regions of Mars: Imaging results from Viking 2. Science, 194: 1329-1337.

De Silva, S.L., M.G. Spagnuolo, N.T. Bridges, and J.R. Zimbelman, 2013. Gravel-mantled megaripples of the Argentinean Puna: A model for their origin and growth with implications for Mars, Geological Society of America Bulletin 125(11-12), 1912-1929.

Edgett, K.S. and P.R. Christensen, 1991. The particle size of Martian aeolian dunes, J. Geohpys. Res. 96, E5, 22765-22776.

Ewing, R., A. Peyret, G. Kocurek, and M. Bourke, 2010. Dune-field pattern formation and recent transporting winds in the Olympia Undae Dune Field, North Polar Region of Mars. Journal of Geophysical Research (Planets): doi:10.1029/2009JE003526.

Fenton, L.K., J.L. Bandfield, and A.W. Ward, 2003. Aeolian processes in Proctor crater on Mars: Sedimentary history as analyzed from multiple data sets. J. Geophy. Res., 108(E12): doi:10.1029/JE002015.

Fenton, L.K., A.D. Toigo, M.I. Richardson, 2005. Aeolian processes in Proctor Crater on Mars: Mesoscale modeling of dune-forming winds. J. Geophys. Res. 110. doi:10.1029/2004JE002309.

Fergason, R.L., P.R. Christensen, and H.H. Kieffer, 2006. High-resolution thermal inertia derived from the Thermal Emission Imaging System (THEMIS): Thermal model and applications, J. Geophys. Res., 111, E12004, doi:10.1029/2006JE002735.

Foroutan, M. and J.R. Zimbelman, 2016. Mega-ripples in Iran: A new analog for transverse aeolian ridges on Mars, Icarus 274, 99-105.

Foroutan, M., and J.R. Zimbelman, 2017. Characteristics of More Than One Million TARs on Mars, in: 48th Lunar and Planetary Science Conference. Lunar and Planetary Institute, Houston, p. Abstract #2591.

Geissler, P.E., 2014. The birth and death of transverse aeolian ridges on Mars, J. Geophys. Res. Planets 119(12), 2583-2599.

Geissler, P.E. and J.T. Wilgus, 2017. The morphology of transverse aeolian ridges on Mars, Aeolian Res. 26, 63-71.

Golombek, M., K. Robinson, A. McEwen, N. Bridges, B. Ivanov, L. Tornabene, R. Sullivan, 2010. Constraints on ripple migration at Meridiani Planum from Opportunity and HiRISE observations of fresh craters. J. Geophys. Res. Planets, 115(R00F08), doi: 10.1029/2010JE003628.]

Greeley, R., N. Lancaster, S. Lee and Thomas, P., 1992. Martian Aeolian processes, sediments and features. In: H.H. Kieffer, B.M. Jakosky, C.W. Snyder and M.S. Matthews (Editors), Mars. University of Arizona Press, Tuscon.

Greeley, R., S.W. Squyres, R.E. Arvidson, P. Bartlett, J.F. Bell III, D. Blaney, N.A. Cabrol, J. Farmer, B. Farrand, M.P. Golombek, S.P. Gorevan, J.A. Grant, A.F.C Haldemann, K.E. Herkenhoff, J. Johnson, G. Landis, M.B. Madsen, S.M. McLennan, J. Moersch, J.W. Rice Jr., L. Richter, S. Ruff, R.J. Sullivan, S.D. Thompson, A. Wang, C.M. Weitz, P. Whelley,

and the Athena Science Team, 2004. Wind-related processes detected by the Spirit rover at Gusev crater, Mars. Science, 305: 810-821.

Greeley, R., R.E. Arvidson, P.W. Barlett, D. Blaney, N.A. Cabrol, P.R. Christensen, R.L. Fergason, M.P. Golombek, G.A. Landis, M.T. Lemmon, S.M. McLennan, J.N. Maki, T. Michaels, J.E. Moersch, L.D.V. Neakrase, S.C.R. Rafkin, L. Richter, S.W. Squyres, P.A. de Souza Jr., R.J. Sullivan, S.D. Thompson, and P.L. Whelley, 2006. Gusev crater: Wind-related features and processes observed by the Mars Exploration Rover Spirit. J. Geophy. Res., 111(E02S09): doi: 10.1029/2005JE002491.

Hartmann, W.K., 2005. Martian cratering. 8. Isochron refinement and the history of martian geologic activity. Icarus, 174: 294-320.

Hartmann, W.K., 2007a, Martian chronology: Toward resolution of the 2005 "controversy" and evidence for obliquity-driven resurfacing processes, in *Seventh International Conference on Mars*, abstract 3318, Lunar and Planetary Institute, Houston.

Hartmann, W.K., 2007b, Martian cratering 9: Toward resolution of the controversy about small craters, *Icarus*, *189*, 274-278.

Hayward, R.K., L.K. Fenton, and T.N. Titus, 2014. Mars Global Digital Dune Database (MGD3): Global dune distribution and wind pattern observations. Icarus 230, 38–46. doi:10.1016/j.icarus.2013.04.011.

Hayward, R.K., K.F. Mullins, L.K. Fenton, T.M. Hare, T.N. Titus, M.C. Bourke, A. Colaprete, and P.R. Christensen, 2007. Mars Global Digital Dune Database and initial science results. J. Geophys. Res. 112. doi:10.1029/2007JE002943.

Hugenholtz, C.H., and T.E. Barchyn, 2017. A terrestrial analog for transverse aeolian ridges (TARs): Environment, morphometry, and recent dynamics. Icarus 289, 239–253. doi:10.1016/j.icarus.2016.08.010.

Hugenholtz, C.H., T.E. Barchyn, and A. Boulding, 2017. Morphology of transverse aeolian ridges (TARs) on Mars from a large sample: Further evidence of a megaripple origin?, Icarus 286, 193-201.

Hynek, B.M., and R.J. Phillips, 2008. The stratigraphy of Meridiani Planum, Mars, and implications for the layered deposits' origin, Earth and Planet. Sci. Lett. 274, 214-220.

Jensen H.B. and T.D. Glotch, 2011. Investigation of the near-infrared spectral character of putative Martian chloride deposits, *J. Geophys. Res. 116*, E00J03.

Kerber, L. and J.W. Head, 2012. A progression of induration in Medusae Fossae Formation transverse aeolian ridges: evidence for ancient aeolian bedforms and extensive reworking, Earth Surf. Proc. Landforms 37(4), 422-433.

Kirk, R.L., E. Howington-Kraus, M.R. Rosiek, J.A. Anderson, B.A. Archinal, K.J. Becker, D.A. Cook, D.M. Galuszka, P.E. Geissler, T.M. Hare, I.M. Holmberg, L.P. Keszthelyi, B.L. Redding, W.A. Delamere, D. Gallagher, J.D. Chapel, E.M. Eliason, R. King, and A.S. McEwen, 2008. Ultrahigh resolution topographic mapping of Mars with MRO HiRISE stereo images: Meter-scale slopes of candidate Phoenix landing sites, J. Geophy. Res. 113, E00A24, doi:10.1029/2007JE003000.

Lancaster, N. and R. Greeley, 1987. Morphology of southern hemisphere intracrater dune fields, Reports of planetary geology and geophysics program- 1986. NASA TM89810, pp. 264-265 (abstract).

Lapotre, M.G.A., R.C. Ewing, M.P. Lamb, W.W. Fischer, J.P. Grotzinger, D.M. Rubin, K.W. Lewis, M.J. Ballard, M. Day, S. Gupta, S.G. Banham, N.T. Bridges, D.J. Des Marais, A.A. Fraeman, J.A. Grant, K.E. Herkenhoff, D.W. Ming, M.A. Mischna, M.S. Rise, D.Y. Sumner, A.R. Vasavada, and R.A. Yingst, 2016. Large wind ripples on Mars: A record of atmospheric evolution, Science 353 (6294), 55-58.

Malin, M.C., and K.S. Edgett, 2000. Sedimentary Rocks of Early Mars, Science 290, 1927-1937.

Malin, M.C., J.F. Bell, B.A. Cantor, M.A. Caplinger, W.M. Calvin, R.T. Clancy, K.S. Edgett, L. Edwards, R.M. Haberle, P.B. James, S.W. Lee, M.A. Ravine, P.C. Thomas, and M.J. Wolff, 2007. Context Camera Investigation on board the Mars Reconnaissance Orbiter. J. Geophys. Res. 112. doi:10.1029/2006JE002808.

McCauley, J.F., M.H. Carr, J.A. Cutts, W.K. Hartmann, H. Masursky, D.J. Milton, R.P. Sharp, and D.E. Wilhelms, 1972. Preliminary Mariner 9 report on the geology of Mars. Icarus, 17: 289-327.

McEwen, A.S., and E.B. Bierhaus, 2006. The Importance of Secondary Cratering to Age Constraints on Planetary Surfaces. Annu. Rev. Earth Planet. Sci. 34, 535–567. doi:10.1146/annurev.earth.34.031405.125018

Montgomery, D.R., J.L. Bandfield, and S.K. Becker, 2012. Periodic bedrock ridges on Mars, J. Geophys. Res. 117, E03005, doi:10.1029/2011JE003970.

Putzig, N.E., M.T. Mellon, 2007. Apparent thermal inertia and the surface heterogeneity of Mars, Icarus, 191, 68-94, doi:10.1016/j.icarus.2007.05.013.

Rafkin, S., B. Haberle, and T. Michaels, 2001. The Mars regional atmospheric modelling system: Model description and selected simulations. Icarus, 151: 228-256.

Rafkin, S. and T. Michaels, 2003. Meteorological predictions for the 2003 Mars Exploration Rover high-priority landing sites. J. Geophy. Res., 108(E12): doi:10.1029/2002JE002027.

Ramsey, M., P. Christensen, N. Lancaster, and D. Howard, 1999. Identification of sand sources and transport pathways at the Kelso Dunes, California, using thermal infrared remote sensing, GSA Bulletin 111 (5). 646-662.

Reiss, D., S. van Gasselt, G. Neukum, and R. Jaumann, 2004. Absolute dune ages and implications for the time of formation of gullies in Nirgal Vallis, Mars. J. Geophy. Res., 109(E06): doi:10.1029/2004JE002251.

Salvatore, M.R., 2008. Global survey of Martian Transverse Aeolian Ridges, Planetary Dunes Workshop: A Record of Climate Change (Lunar and Planetary Institute), Alamogordo, New Mexico (print only abstract).

Sharp, R.P., 1963. Wind ripples. J. Geology, 71: 617-636.

Shockey, K.M. and J.R. Zimbelman, 2013. Analysis of transverse aeolian ridge profiles derived from HiRISE images of Mars, Earth Surf. Proc. and Landforms 38(2), 179-182.

Silvestro, S., G. Di Achille, and G.G. Ori, 2010. Dune morphology, sand transport pathways and possible source areas in east Thaumasia Region (Mars). Geomorphology 121, 84–97. doi:10.1016/j.geomorph.2009.07.019.

Sullivan, R., D. Banfield, J.F. Bell III, W. Calvin, D. Fike, M. Golombek, R. Greeley, J. Grotzinger, K. Herkenhoff, D. Jerolmack, M. Malin, D. Ming, L.A. Soderblom, S.W. Squyres, S. Thompson, W.A. Watters, C.M. Weitz, and A. Yen, 2005. Aeolian processes at the Mars Exploration Rover Meridiani Planum landing site, Nature 436(7047), 58.

Sullivan, R., R. Arvidson, J.F. Bell III, R. Gellert, M. Golombek, R. Greeley, K. Herkenhoff, J. Johnson, S. Thompson, P. Whelley, and J. Wray, 2008. Wind-driven particle mobility on

Mars: Insights from Mars Exploration Rover observations at "El Dorado" and surroundings at Gusev Crater, J. Geophys. Res., 113, E06S07, doi:10.1029/2008JE003101.

Sullivan, R., N. Bridges, K. Herkenhoff, V. Hamilton, and D. Rubin, 2014. Transverse Aeolian Ridges (TARs) as megaripples: Rover encounters at Meridiani Planum, Gusev, and Gale, *8th Int'l Conf. on Mars*, abstract 1424.

Thomas, P., 1981. North-south asymmetry of eolian features in Martian polar regions: Analysis based on crater-related wind markers. Icarus, 48: 76-90.

Thomas, P.C., M.C. Malin, M.H. Carr, and G.E. Danielson, 1999. Bright dunes on Mars. Nature, 397: 592-594.

Tirsch, D., 2009. Dark dunes on Mars: Analyses on origin, morphology, and mineralogical composition of dark material in Martian craters. DLR-Forschungsbericht. DLR-FB 2009-08, 166 p.

Tirsch, D., R. Jaumann, A. Pacifici, F. Poulet, 2011. Dark aeolian sediments in Martian craters: Composition and sources, J. Geophys. Res. Planets, 116(E3), doi: 10.1029/2009JE003562.

Tsoar, H., R. Greeley, and A.R. Peterfreund., 1979. Mars: The north polar sand sea and related wind patterns. J. Geophy. Res., 84: 8167-8180.

Wells, G.L. and J.R. Zimbelman, 1997. Extraterrestrial arid surface processes. In: D.S.G. Thomas (Editor), Arid Zone Geomorphology: Processes, Form and Change. John Wiley and Sons, New York.

Wilson, S.A. and J.R. Zimbelman, 2004. The latitude dependent nature and physical characteristics of transverse aeolian ridges on Mars. J. Geophy. Res., 109(E10): doi:10.1029/2004JE002247.

Zimbelman, J.R., 1987. Spatial resolution and the geologic interpretation of martian morphology: Implications for subsurface volatiles. Icarus, 71: 257-267.

Zimbelman, J.R., 2008. Transverse Aeolian Ridges on Mars: results obtained from analysis of HiRISE images, Planetary Dunes Workshop: A Record of Climate Change (Lunar and Planetary Institute), Alamogordo, New Mexico.

Zimbelman, J.R., 2010. Transverse Aeolian Ridges on Mars: First results from HiRISE images, Geomorphology, doi:10.1016/j.geomorph.2009.05.012.

Zimbelman, J.R. and S.H. Williams, 2007. Dunes versus ripples: topographic profiling across terrestrial examples, with application to the interpretation of features on Mars, pp. P34A-07.

Zimbelman, J.R. and S.P. Scheidt, 2014. Precision topography of a reversing sand dune at Bruneau Dunes, Idaho, as an analog for Transverse Aeolian Ridges on Mars, Icaurs 230, 29-37.

Zimbelman, J.R., S.H. Williams, and A.K. Johnston, 2012. Cross-sectional profiles of sand ripples, megaripples, and dunes: a method for discriminating formational mechanisms, Earth Surf. Process. Landforms 37, 1120-1125.

Zimbelman, J.R., M.C. Bourke, and R.D. Lorenz, 2013. Recent developments in planetary Aeolian studies and their terrestrial analogs, Aeolian Res. 11, 109-126.

Figure Captions:

Figure 1. a) Simple TARs with interspersed boulders on the floor of Proctor crater (HiRISE image ESP_011909_1320). b) LDDs on the floor of Proctor crater lying on top of a sea of saturated TARs (HiRISE image ESP_011909_1320). c) Dark aeolian material filling in pits within light-toned deposits in Meridiani Planum (HiRISE image PSP_006860_1840). d) Example of light-toned layered deposits above TARs on the floor of Schiaparelli crater (HiRISE image ESP_032335_1760). Note the secondary ridges perpendicular to the TAR crests.

Figure 2. Mars Global Surveyor (MGS) Mars Orbiter Laser Altimeter (MOLA) 256 pixel/degree color hillshade map showing locations of six study areas (red boxes), each five by five degrees in size.

Figure 3. Examples of elevation profiles of single TAR bedforms drawn on DTMs. a) Elevation profile showing measurements of TAR height and width. b) Elevation profile showing measurement of symmetry distance.

Figure 4. Mapping results for Study Area 1 covering Proctor crater over a THEMIS IR daytime base. a) Map of TAR deposits (either patchy or saturated), LDDs, dark aeolian deposits, and layered terrains. Colors are transparent so overlapping polygons may show blended colors. Bright green arrows represent potential sediment pathways for TARs. Scale bar also applies to b and c. b) Map of dominant TAR morphology per 15x15 km grid. Location of d shown by white box. c) Map of dominant TAR orientation per 15x15 km grid. Orientation of colored lines aligns

with dominant orientation of TAR ridge crests and perpendicular to inferred dominant wind direction. d) CTX image P13_006134_1332 showing some of the larger pits on the western floor of Proctor crater. Locations of e and f shown by white boxes. e) HiRISE image of layered pits with dark aeolian material eroding from layers and TARs overlaying polygonal light toned terrains (ESP_020256_1320). f) Closeup of HiRISE image ESP_020256_1320 showing light-toned polygons breaking into large boulders.

Figure 5. Mapping results for Study Area 2 covering Kaiser crater over a THEMIS IR daytime base. a) Map of TAR deposits (either patchy or saturated), LDDs, dark aeolian deposits, and layered terrains. b) Map of TAR morphology. Location of d shown in white box. c) Map of TAR orientations. d) CTX image B16_015984_1348 showing mount of light-toned material surrounded by LDDs. Locations of e and f shown in white boxes. e) HiRISE image of light-toned mound material. Note absence of material on western sides of TARs (PSP_006609_1330). f) Partial color HiRISE image showing what may be TAR forming material being transported east to west, some emanating from light toned deposits (black arrows; ESP_046181_1325).

Figure 6. Mapping results for Study Area 3 covering Meridiani Planum over a THEMIS IR daytime base. a) Map of TAR deposits (either patchy or saturated), LDDs, dark aeolian deposits, and layered terrains. b) Map of dominant TAR morphology per 15x15 km grid. Locations of d-f shown in white boxes. c) Map of dominant TAR orientation per 15x15 km grid. Orientation of colored lines aligns with dominant orientation of TAR ridge crests. d) Color HiRISE image showing light toned and layered terrains superposed by saturated barchan-like and simple TARs. Note that TARs at north end change in morphology and wavelength from left to right due to

topographic obstacles. (PSP_001493_1815). e) Color HiRISE images of a saturated barchan-like TAR deposit in Meridiani Planum overlaying polygonal light toned terrain (PSP_005647_1815). Note that chains of larger TARs resemble large simple TARs perpendicular to their true orientation at lower resolutions. f) Crater impacted into light-toned layered terrain showing dark aeolian material emanating from layers (HiRISE image PSP_006570_1820).

Figure 7. Mapping results for Study Area 4 covering the western portion of Schiaparelli crater over a THEMIS IR daytime base. a) Map of TAR deposits (either patchy or saturated), LDDs, dark aeolian deposits, and layered terrains. b) map of TAR morphology. Locations of d-f shown in white boxes. c) map of TAR orientations. d) TARs overlying light-toned layered terrains, showing the complex relationship between the two (HiRISE color image ESP_032335_1760). e) Close view of primary TAR bedforms (ridges running roughly north to south) with perpendicular secondary ridges and visible tertiary ridges perpendicular to the secondary ridges (HiRISE image ESP_028788_1760). f) Light-toned layered knobs surrounded by TARs and dark aeolian material (ESP_032335_1760).

Figure 8. Mapping results for Study Area 5 covering Dawes crater over a THEMIS IR daytime base. a) Map of TAR deposits (either patchy or saturated), LDDs, dark aeolian deposits, and layered terrains. b) Map of TAR morphology. Location of d shown in white box. c) Map of TAR orientations. d) Example of “feathered” TARs (HiRISE image ESP_028774_1705).

Figure 9. Mapping results for Study Area 6 covering Moreux crater over a THEMIS IR daytime base. a) Map of TAR deposits (either patchy or saturated), LDDs, dark aeolian deposits, and

layered terrains. b) Map of TAR morphology. Location of d shown in white box. c) Map of TAR orientations. d) LDDs overlying patchy TAR deposits. Note the large dune ripples abutting the TARs in some places with different orientations due to the fact that they are more active and thus subject to current wind regimes. (HiRISE image ESP_025714_2220).

Figure 10. a) Plot of width versus height/width measurements of terrestrial duneforms (solid symbols, adapted from Zimbelman et al. (2012) and TARs from DTMs (hollow symbols, mean values of all TARs from each DTM plotted with standard deviations of those values as bars, this study). TARs lie in between the terrestrial features, but most closely match transverse dunes or pebble-coated megaripples. b) Example TAR heights and widths scaled by max width of profiles from DTMs A and B.

Figure 11. Color altimetry for DTM A in Proctor crater (constructed from HiRISE images ESP_024449_1320 and ESP_024515_1320) superposed on a) HiRISE orthoimage and b) DTM hillshade.

Figure 12. Color altimetry for DTM B in Schiaparelli crater (constructed from HiRISE images ESP_025966_1765 and ESP_026889_1765) superposed on a) HiRISE orthoimage and b) DTM hillshade.

Figure 13. Color altimetry for DTM C in Schiaparelli crater (constructed from HiRISE images PSP_007822_1775 and PSP_008178_1775) superposed on a) HiRISE orthoimage and b) DTM hillshade.

Figure 14. Color altimetry for DTM D in Kaiser crater (constructed from HiRISE images PSP_006820_1325 and ESP_033047_1325) superposed on a) HiRISE orthoimage and b) DTM hillshade.

Figure 15. Crater count areas (purple polygon) and measured crater diameters (red lines) in Study Area 4 on a) CTX image G04_019597_1766 and HiRISE image ESP_026889_1765 (small rectangular purple polygon), with black box showing location of b. b) Close up of HiRISE image ESP_026889_1765. c) Crater size-frequency distributions for all count areas. Counts from both CTX and HiRISE images converge between ~30 - ~200 meters at ~2 My, based on isochrons from Hartmann (2015). For the Proctor crater TAR sea, where no superposed craters were identified, the age can be no older than ~100,000 y.

Figure 16. CRISM spectra for TARs, LDDs and local bedrock are compared for Study Area 3 (Meridiani Planum). A context map (top left) shows the mapped regions of dunes and layered materials. Three CRISM images are shown (bottom row) in false color for each area. The region of interest from which I/F spectra were extracted is overlaid on each image. Extracted spectra are compared in a plot (top right). CRISM images are approximately 10 km across the narrow part of the scene. CRISM images used include FRT000080c0, FRT000a0ac and FRT0000cc22.

Figure 17. CRISM analyses of light-toned deposits (FRT000094EE) and LDDs (HRL00012403) are compared for materials on the floor of Kaiser crater in Study Area 2. A context image (top left) shows the locations of CRISM images. The regions of interest are shown on each CRISM

false color image. Extracted spectra are compared in a plot at the right. TARs in an around a small unnamed crater have spectral character very similar to that of the local bedrock. LDDs have a strong “blue” slope, which could be an indication of grain coatings.

CRISM images are approximately 10 km across the narrow part of the scene.

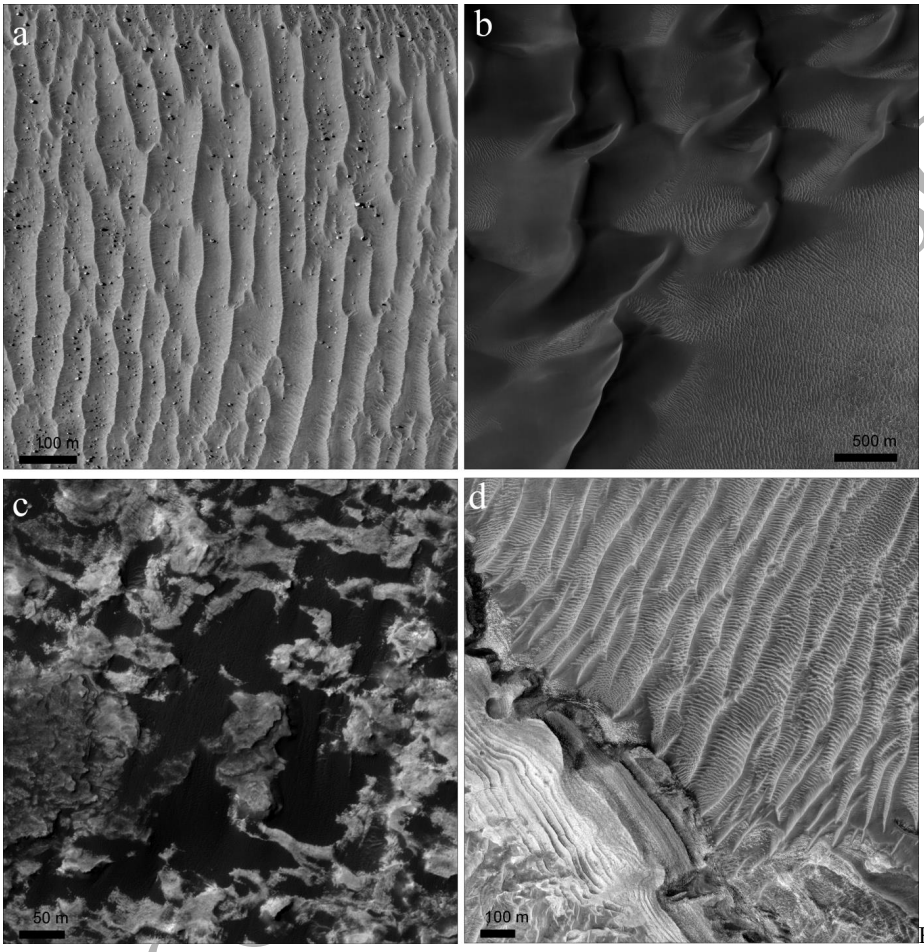

Figure 1

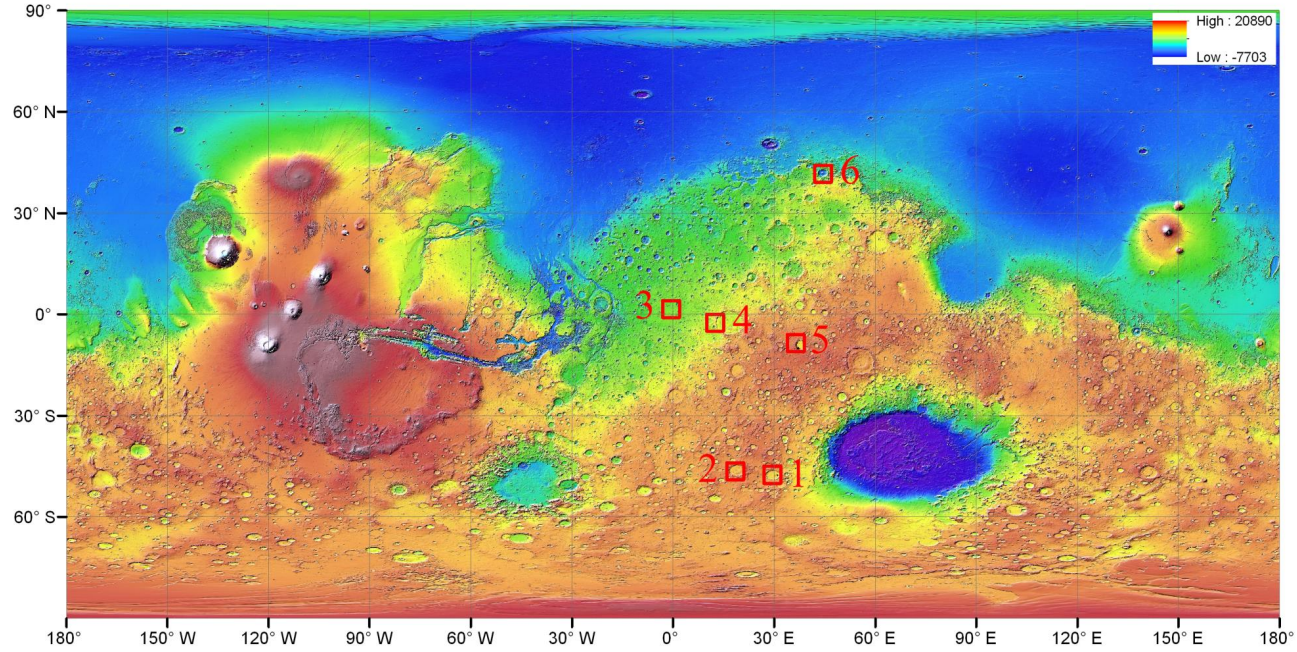

Figure 2.

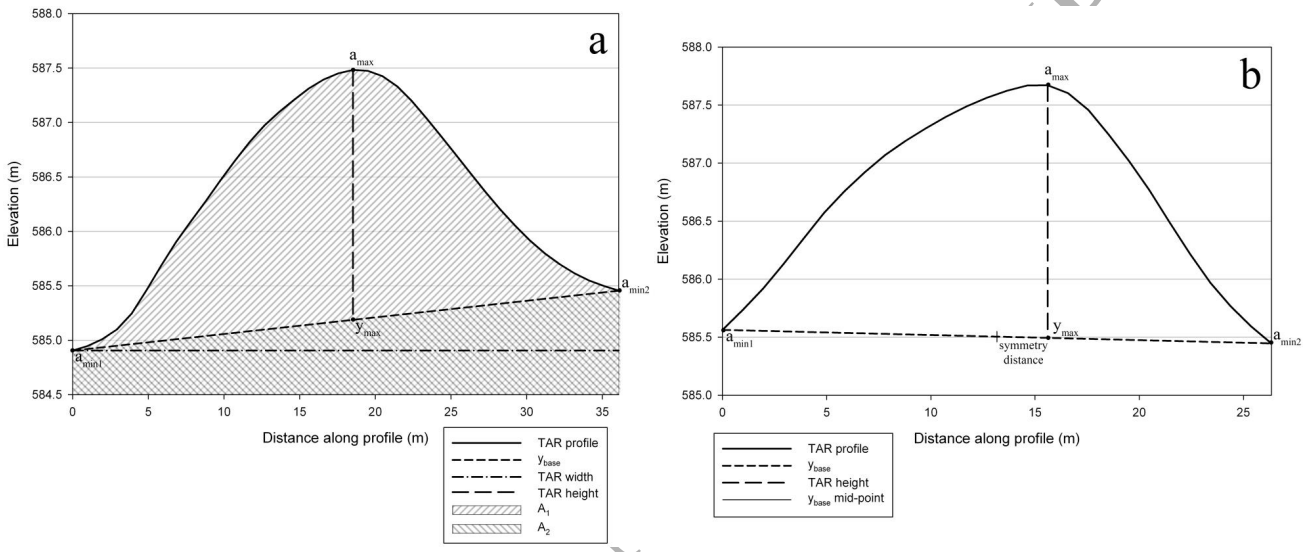

Figure 3.

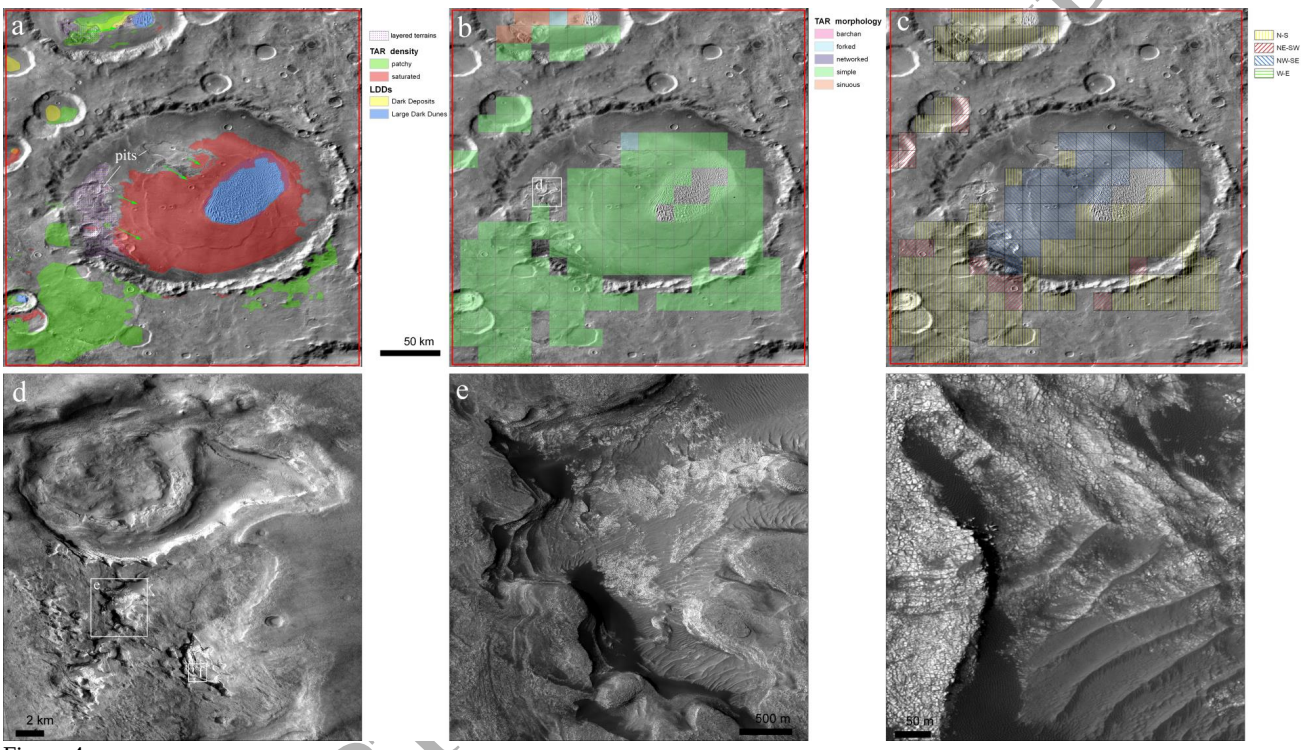

Figure 4.

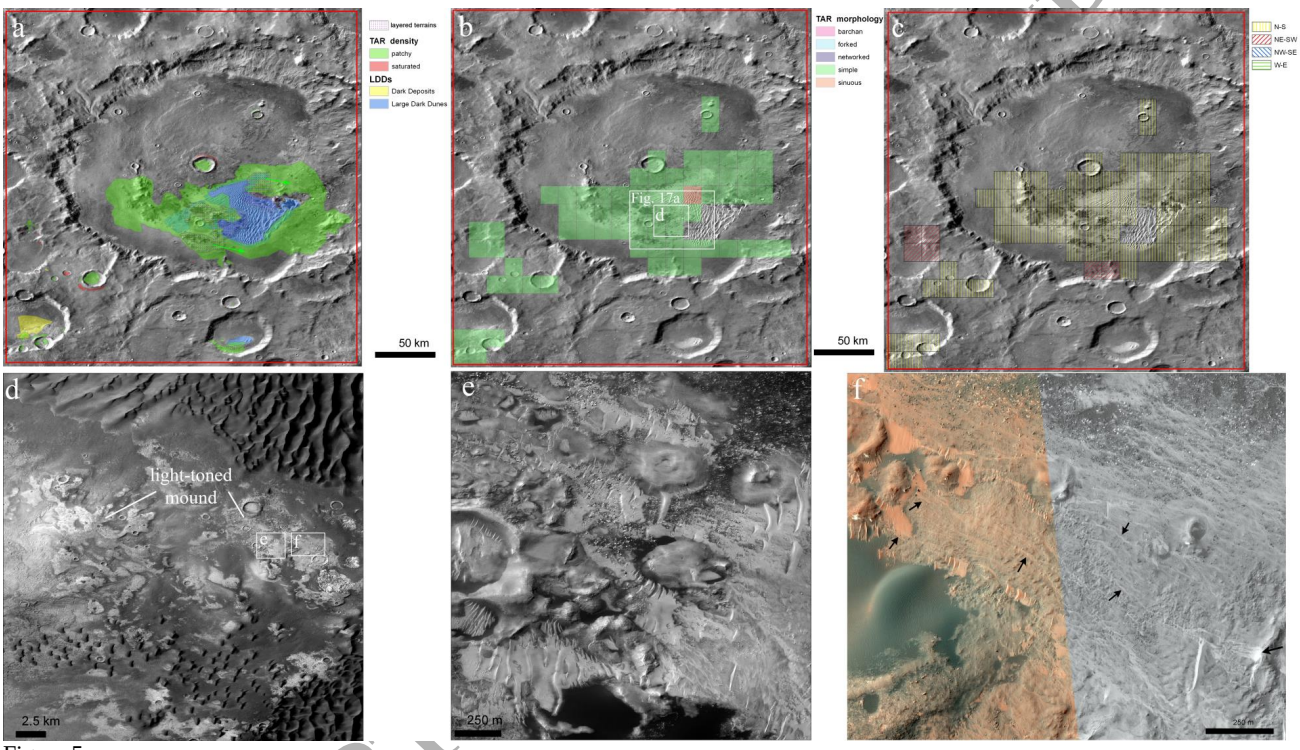

Figure 5.

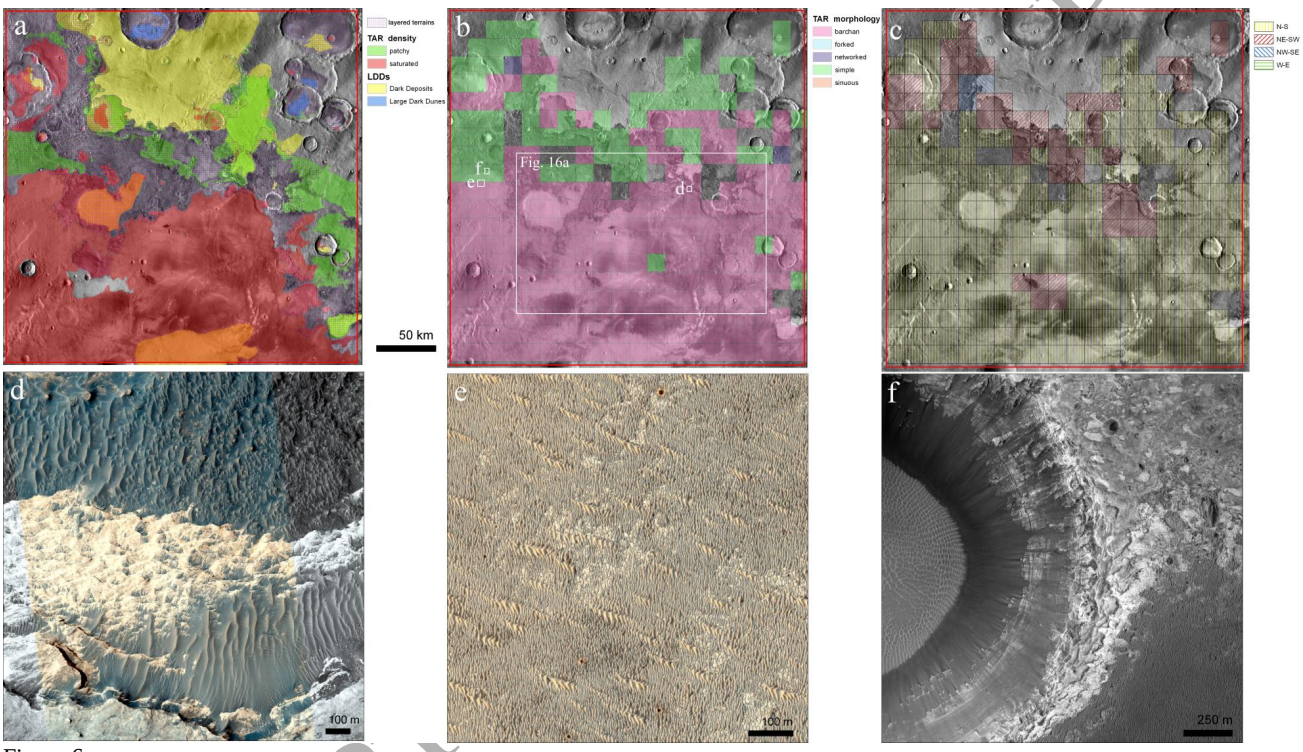

Figure 6.

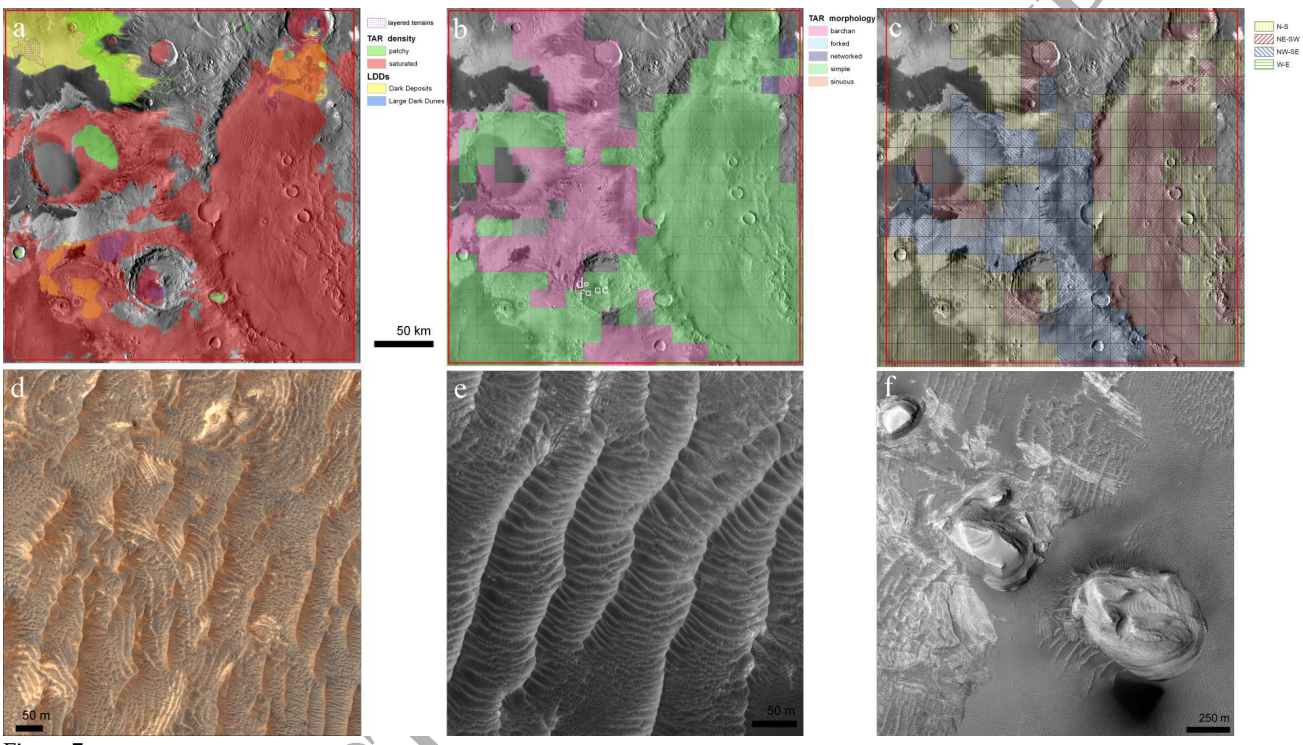

Figure 7.

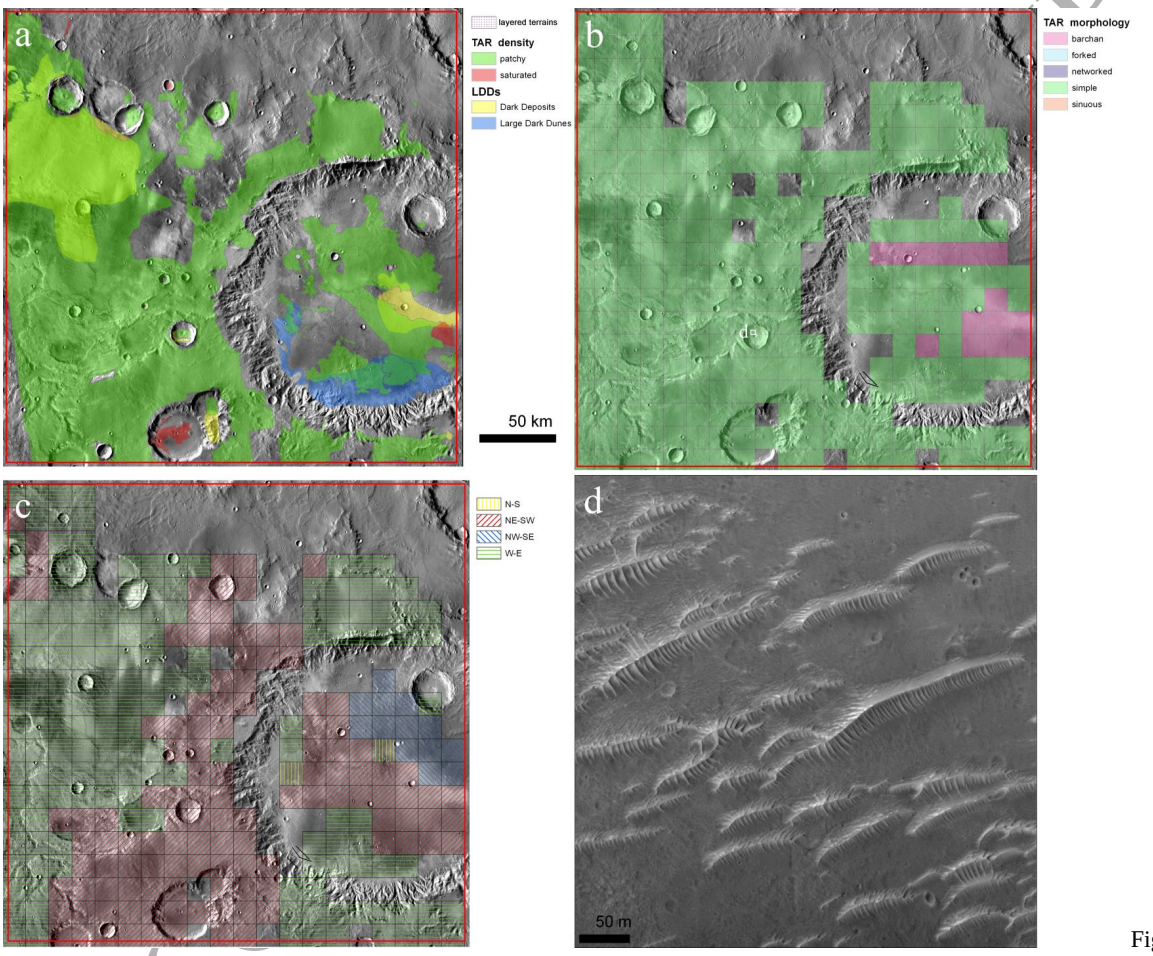
a
layered terrains
TAR density
patchy
saturated
LDDs
Dark Deposits
Large Dark Dunes
50 km
b
TAR morphology
barchan
forked
networked
simple
sinuous
c
N-S
NE-SW
NW-SE
W-E
d
50 m

Figure 8.

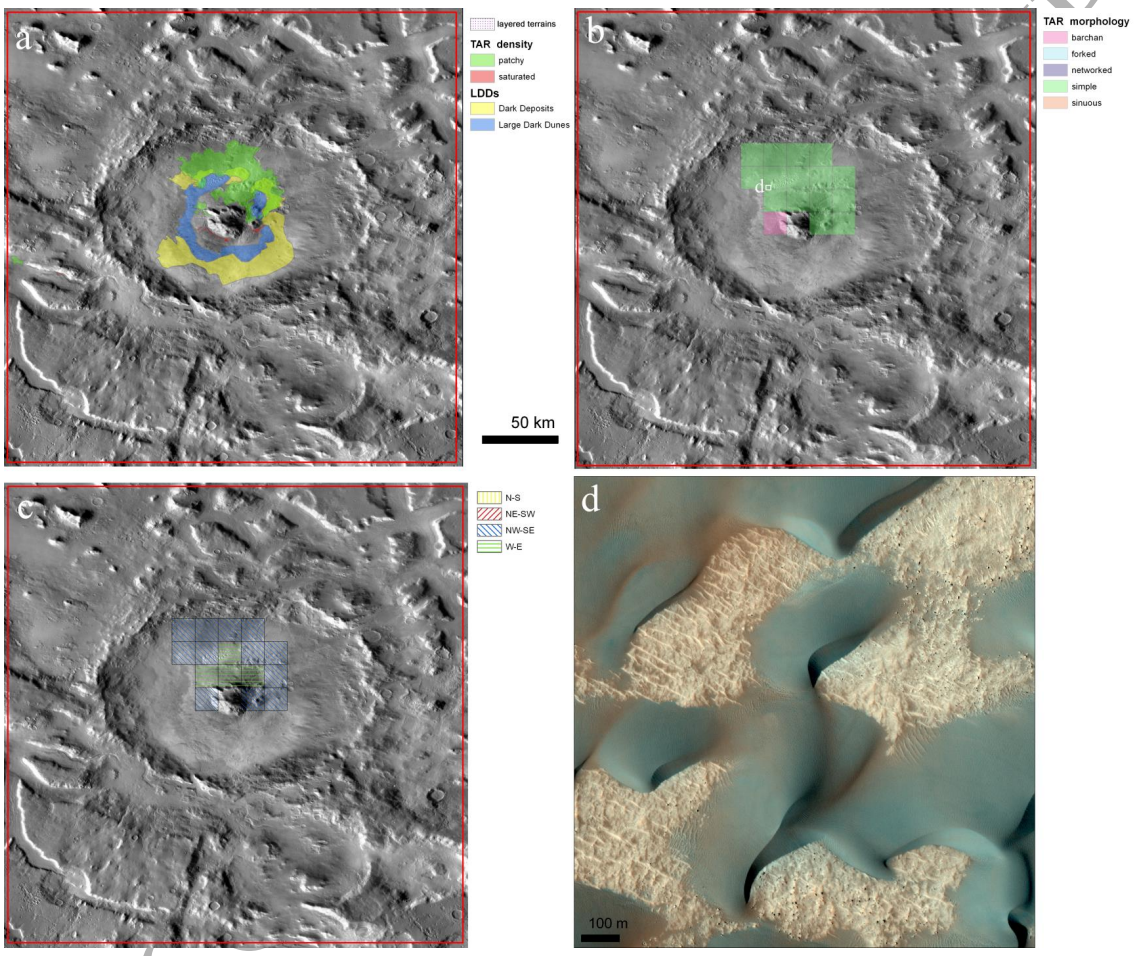
a
layered terrains
TAR density
patchy
saturated
LDDs
Dark Deposits
Large Dark Dunes
50 km
b
TAR morphology
barchan
forked
networked
simple
sinuous
c
N-S
NE-SW
NW-SE
W-E
d
100 m

Figure 9.

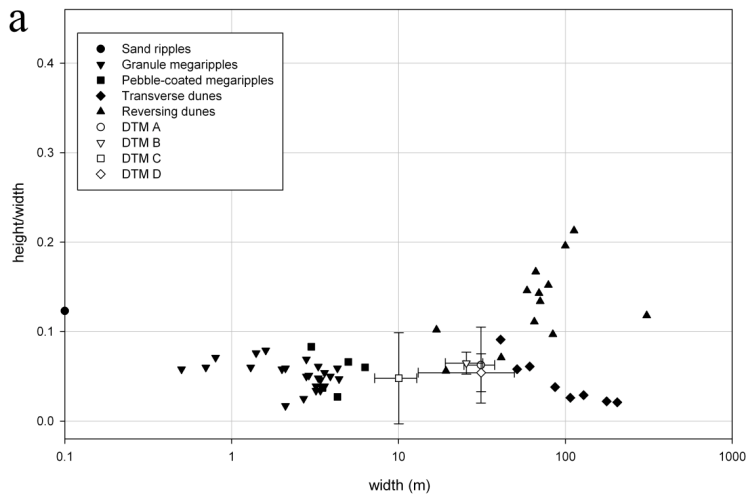
a
Sand ripples
Granule megaripples
Pebble-coated megaripples
Transverse dunes
Reversing dunes
DTM A
DTM B
DTM C
DTM D
height/width
0.0
0.1
0.2
0.3
0.4
0.1
1
10
100
1000
width (m)

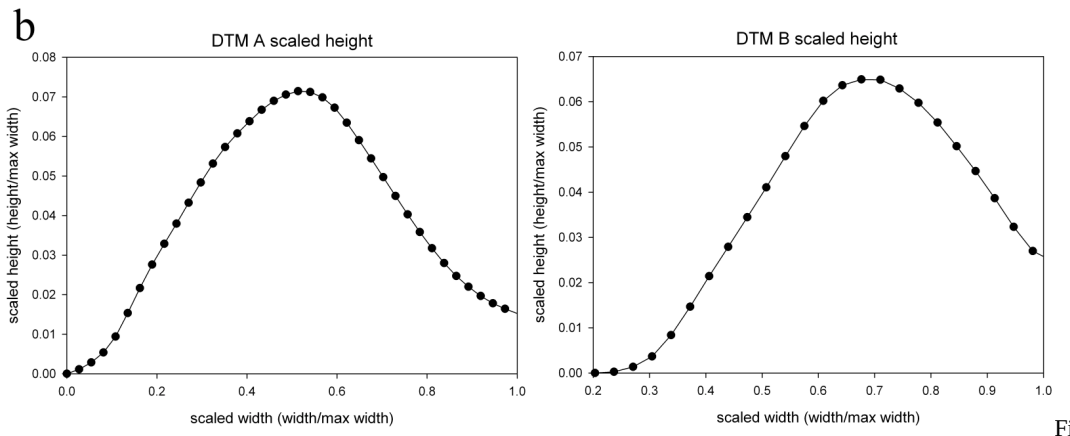
b
DTM A scaled height
scaled height (height/max width)
0.00
0.01
0.02
0.03
0.04
0.05
0.06
0.07
0.08
0.0
0.2
0.4
0.6
0.8
1.0
scaled width (width/max width)
DTM B scaled height
scaled height (height/max width)
0.00
0.01
0.02
0.03
0.04
0.05
0.06
0.07
0.2
0.3
0.4
0.5
0.6
0.7
0.8
0.9
1.0
scaled width (width/max width)

Figure 10.

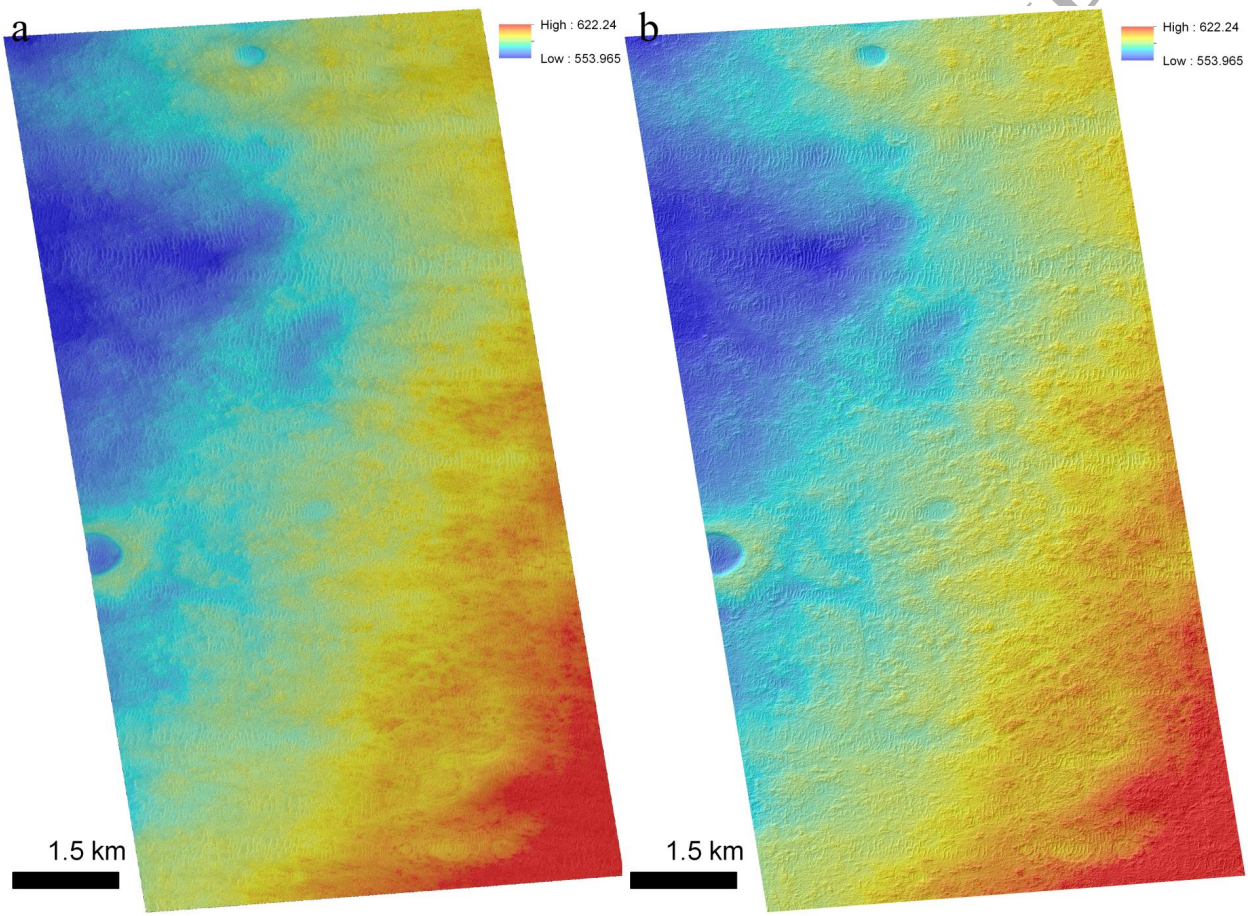

Figure 11.

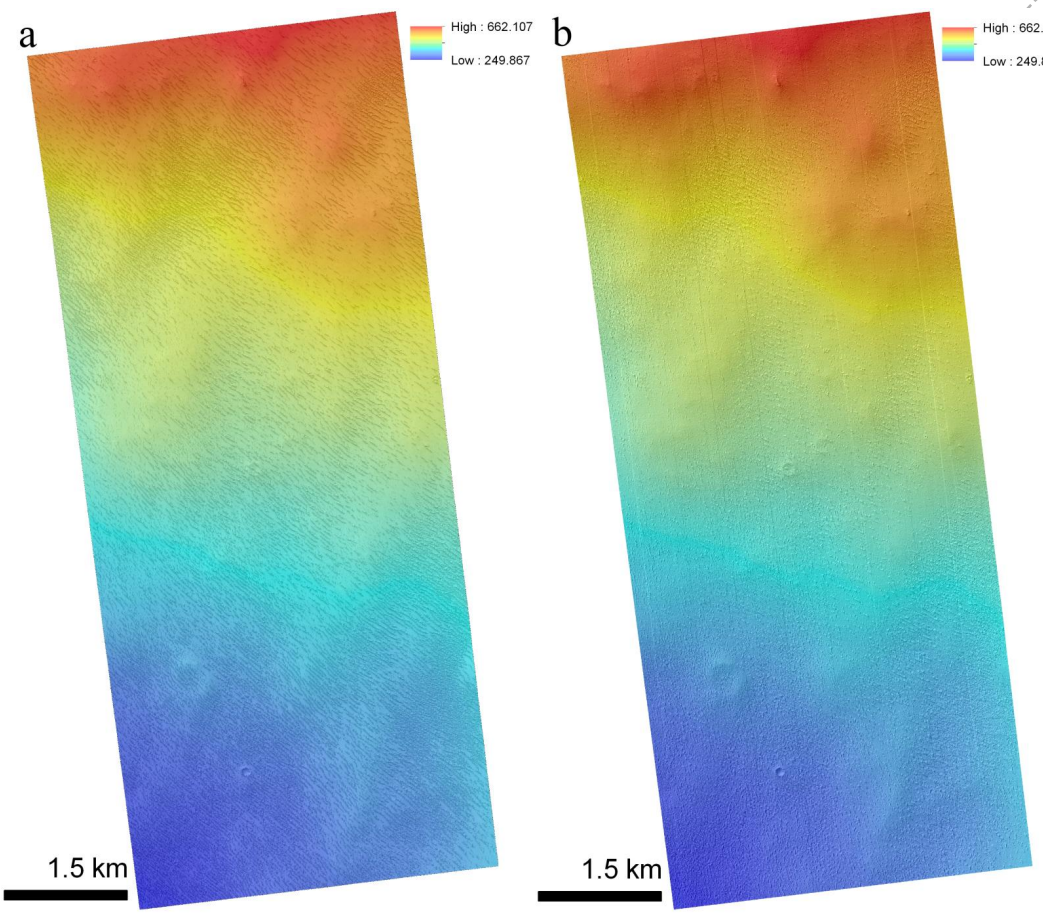

Figure 12.

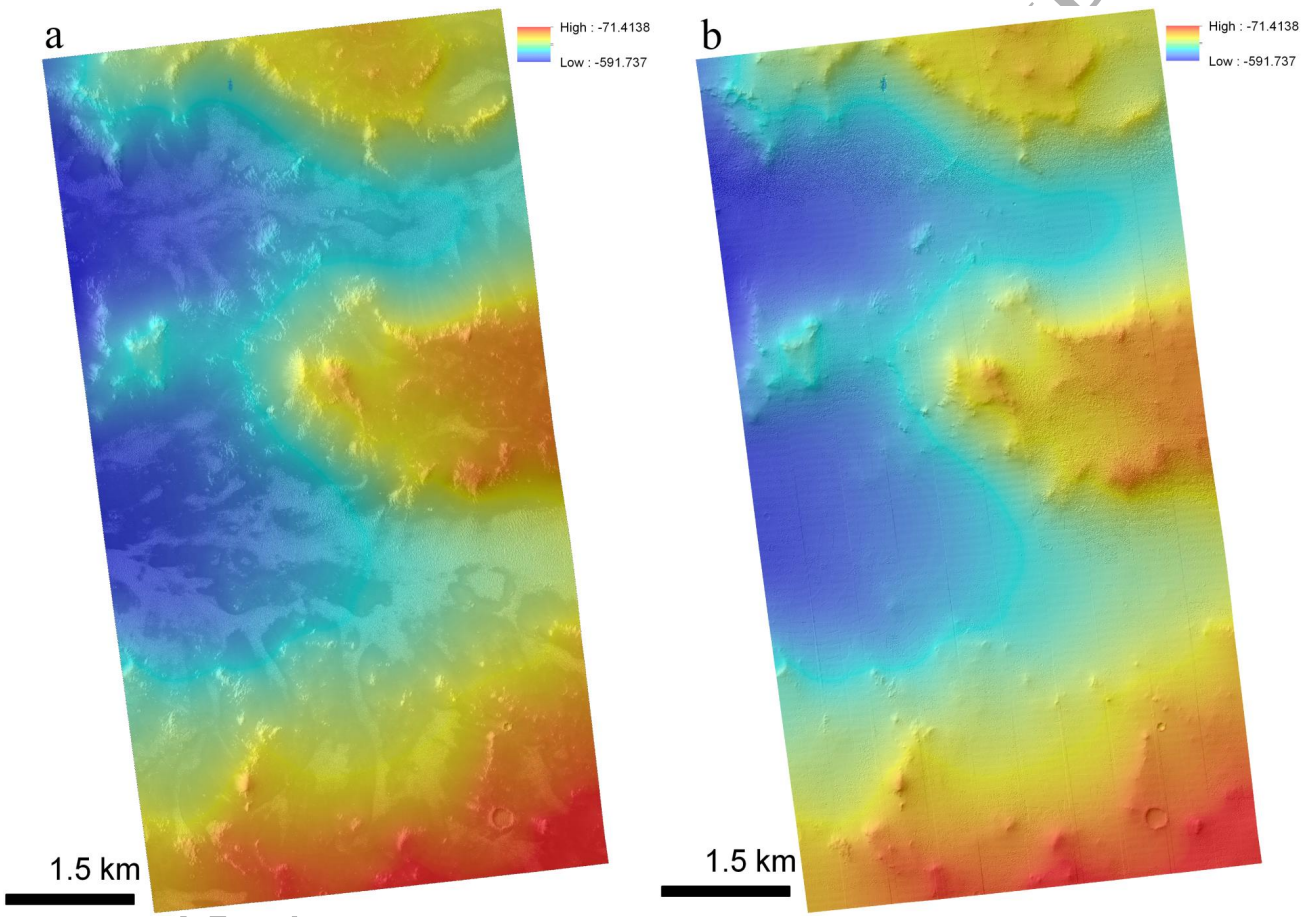

Figure 13.

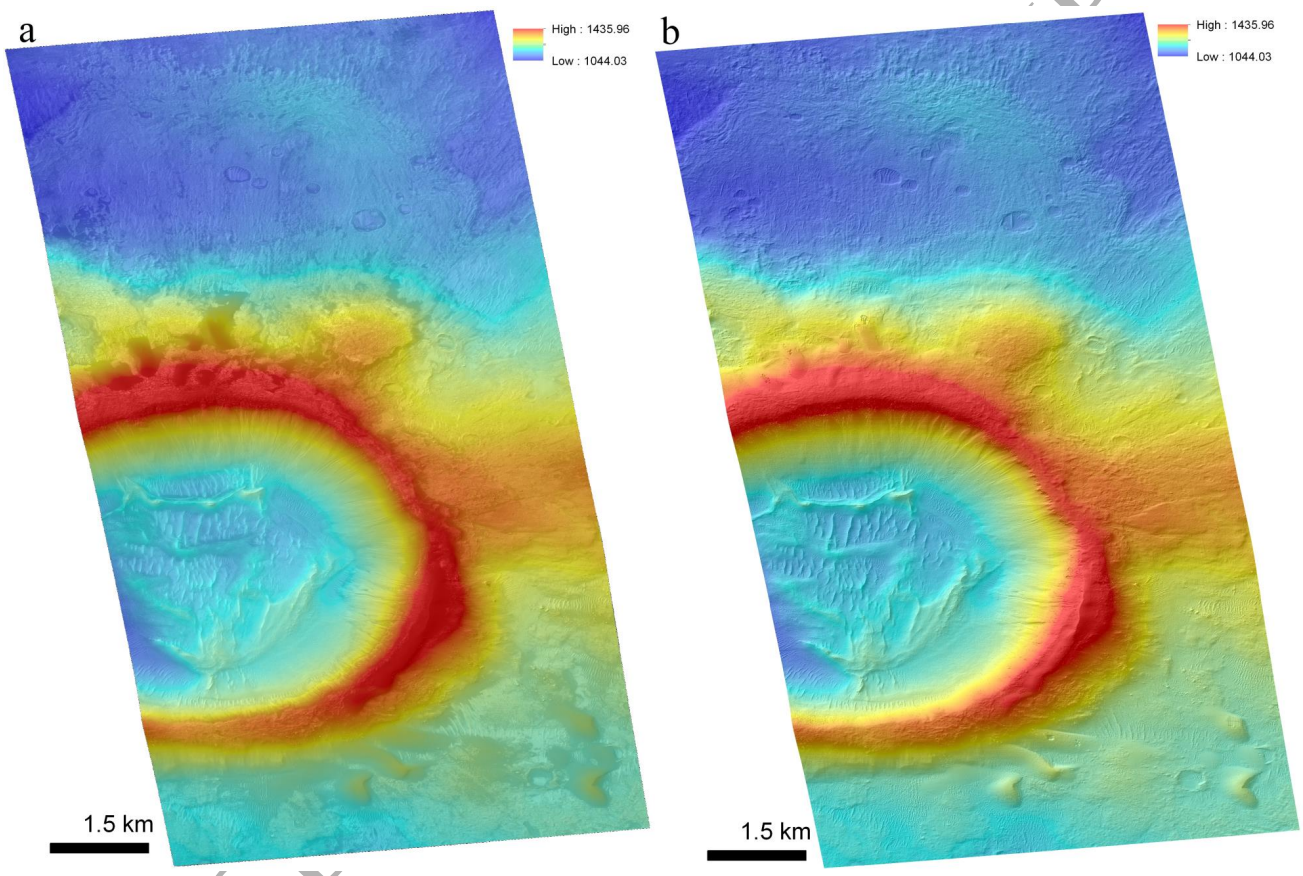

Figure 14.

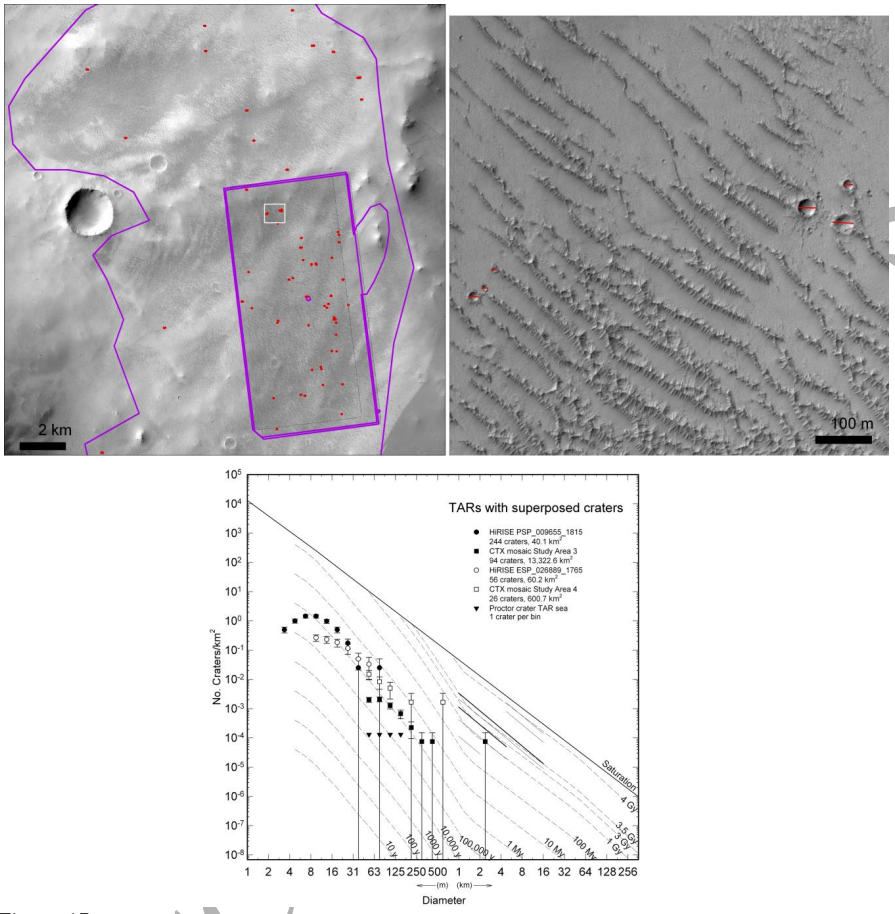
2 km
100 m
TARs with superposed craters
HiRISE PSP_009655_1815
244 craters, 40.1 km²
CTX mosaic Study Area 3
94 craters, 13,322.6 km²
HiRISE ESP_026889_1765
56 craters, 60.2 km²
CTX mosaic Study Area 4
26 craters, 600.7 km²
Proctor crater TAR sea
1 crater per bin
No. Craters/km²
Diameter
(m) (km)
Saturation
4 Gy
3.5 Gy
1 Gy
10 My
100 My
1 My
10 ky
100 ky
1000 y
10,000 y
100,000 y

Figure 15.

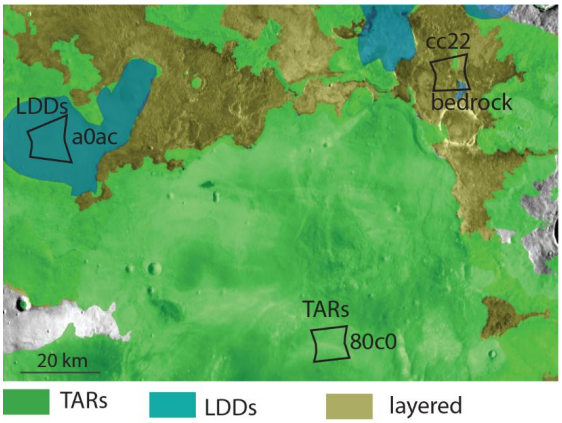
cc22
bedrock
LDDs
a0ac
TARs
80c0
20 km
TARs
LDDs
layered

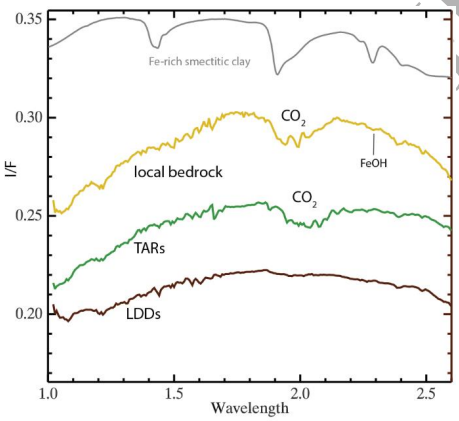
0.35
0.30
0.25
0.20
I/F
Fe-rich smectitic clay
CO2
FeOH
local bedrock
CO2
TARs
LDDs
1.0
1.5
2.0
2.5
Wavelength

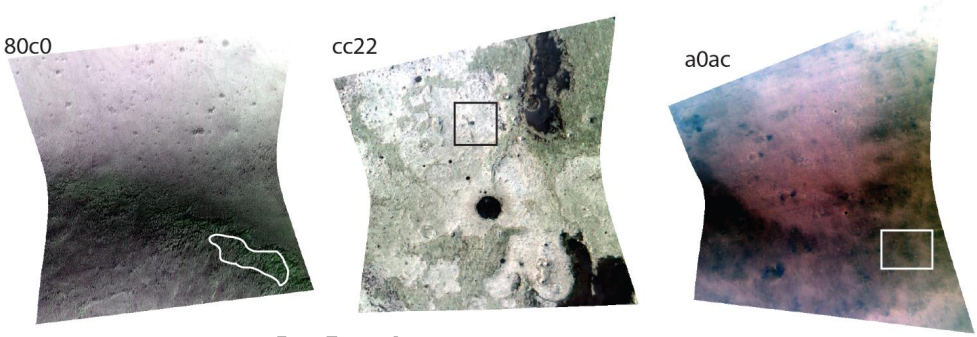
80c0
cc22
a0ac

Figure 16.

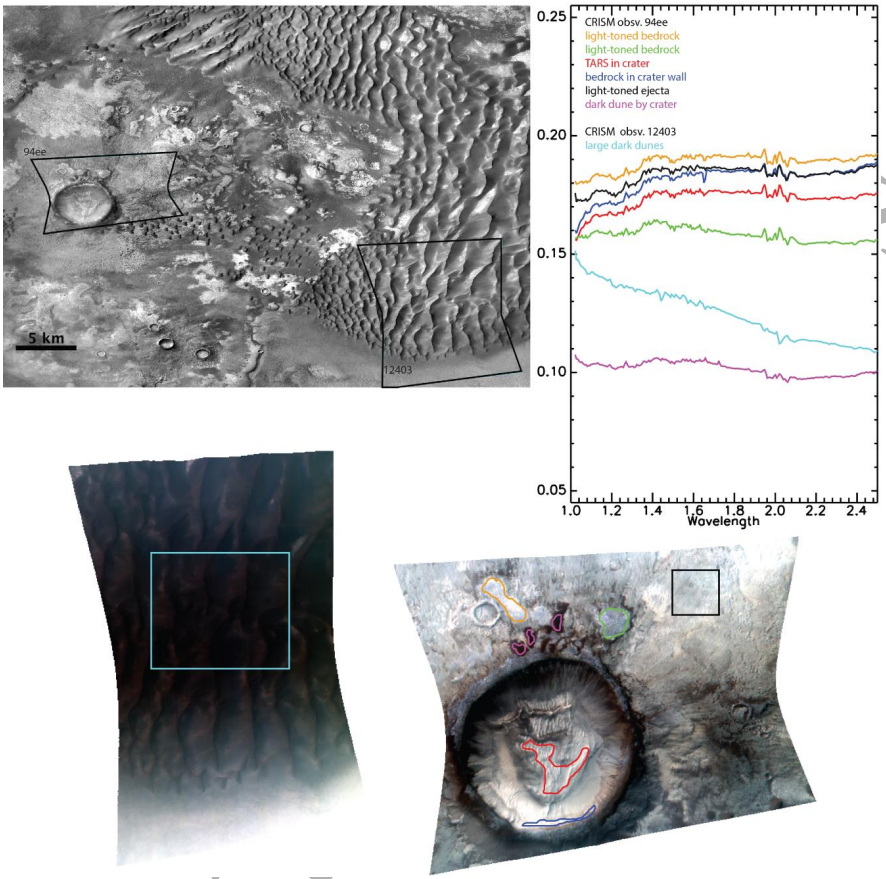
94ee
5 km
12403
CRISM obsv. 94ee
light-toned bedrock
light-toned bedrock
TARS in crater
bedrock in crater wall
light-toned ejecta
dark dune by crater
CRISM obsv. 12403
large dark dunes
0.25
0.20
0.15
0.10
0.05
1.0
1.2
1.4
1.6
1.8
2.0
2.2
2.4
Wavelength

Figure 17.